University of Twente

Ellipsometric study on gaseous layers at the solid/water interface

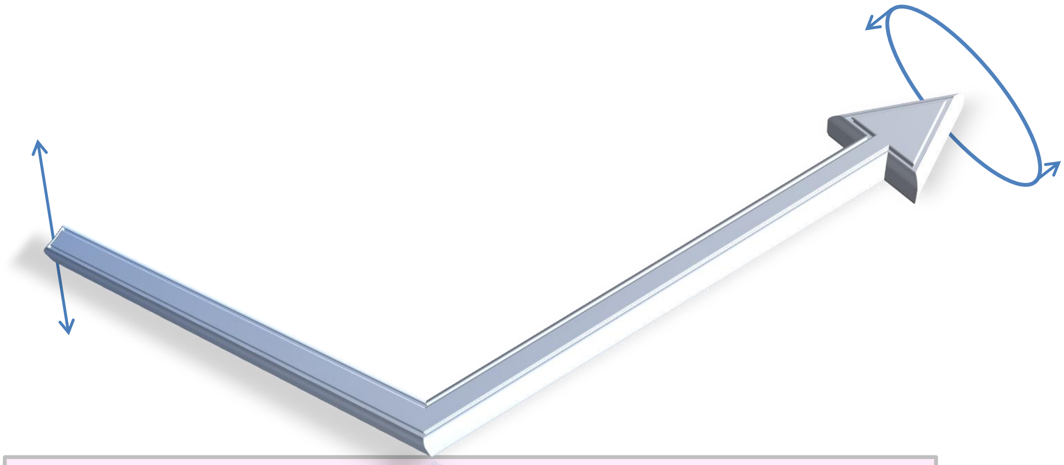

Author: Hüseyin Ateşçi
Supervisor: Dr. ir. Herbert Wormeester
Dr. J.R.T. Seddon
Physics of Interfaces and Nanomaterials Group
Faculty of Science and Technology
MESA+ Institute for Nanotechnology
Submitted July 8, 2013

Abstract

In this thesis, ellipsometry was used to investigate whether gas-enrichment occurs at the solid/water interface, and whether there is a difference in enrichment between hydrophilic and hydrophobic samples. The samples used were silicon with 277 nm thermal oxide on top (hydrophilic) and an additional silicone oil coating (hydrophobic). The samples were held in a liquid cell which could be filled with degassed, He-saturated, and N_2-saturated water. The SiO_2 thickness was taken as the fit parameter. Long (>300 minutes) dynamic scans were made on hydrophobic and hydrophilic samples in different water ambients. It was found that it is likely that gas-enrichment occurs at the solid/water interface due to the qualitative difference observed in the fitted SiO_2 thickness over time between degassed and He-saturated water ambients. This change was noticeable in the first 150 minutes of measurement and was observed for both hydrophilic and hydrophobic samples. In the long term, the fitted SiO_2 always increased, which is unlikely to be caused by gas-adsorption through diffusion, but likely to be caused by contaminants. The hydrophilic samples generally showed a larger change in the fitted SiO_2 thickness than the hydrophobic samples. The exact reason why this happens is unclear, although it could be attributed to the tendency of hydrophilic silicon oxide to be easily contaminated.

Table of contents

1. Introduction

For all its importance, water is still not fully understood scientifically. It exhibits in many aspects a different behavior compared to other liquids. One of the aspects where our understanding of water is limited is when water comes into contact with a surface. What really happens with the system at the nanometer scale? Water in its liquid form consists of a very dynamic network of hydrogen bonds, but, when in close contact with a surface, the amount of hydrogen bonds that can be made with the surface determines its hydrophobicity. Hydrophilic surfaces will tend to be terminated with -OH groups which can form hydrogen bonds with water molecules, this will cause water to maximize its contact surface with the hydrophilic substrate. On the other hand, hydrophobic surfaces do not form hydrogen bonds with water, which will cause the network of hydrogen bonds to be disrupted. Water will in turn maximize its contact angle with the surface [1]. It does not end here, however. On hydrophobic substrates, the density of water molecules drops sharply at to the solid/water interface, leading to a depletion layer [2,3-7,8,9]. Gas molecules can fill this depleted zone of water, which is then termed "gas-enriched depletion layer" [10,4,5,7]. Also, additional structures have been discovered recently on substrates that have been wetted: nanobubbles and micropancakes [11-14,15,16,17]. These intriguing topics shall be discussed briefly. It should also be mentioned that what is meant with (nanoscopic) gaseous domains are gas-enriched depletion layers, nanobubbles, and micropancakes. We will first discuss the first aspect.

When a hydrophobic surface is covered with water, the density of water in the direct vicinity of a hydrophobic surface drops sharply. The theoretical groundwork of this phenomenon was first introduced by Stillinger [18] in 1973. Since then, Barrat *et al.* investigated the solid/water interface system with molecular dynamics simulations. They saw a region of depleted density close to the hydrophobic surface of at least one molecule diameter in thickness, with density fluctuations reaching at least 5 molecule diameters into the bulk liquid [19]. Huang *et al.* performed a molecular dynamics study on a similar system, and found a vapor layer of approximately 0.3 nm in thickness around hydrophobic objects [20]. Wallqvist *et al.* have also observed a vapor layer in a similar research [21]. The thickness of the water vapor layer was reported to be 0.4 nm for a purely repulsive solid/water interaction. Dammer *et al.* predicted that there would be a strong reduction in the density of the Lennard-Jones fluid, which simulated water, near hydrophobic surfaces with density fluctuations with a thickness of as much as 5-10 water molecules [7].

Understanding the physics of the solid/water interface at the nanoscale is important from a fundamental point of view. Hydrophobic spheres in a solution have been used as a simple model to explain phenomena such as protein folding [20]. Understanding depletion layers, whether they are filled with gas or not, is critical for explaining chemical reactions in a liquid at the solid/water interface. It has also consequences for our understanding of slip boundary conditions of water at the substrate surface [21]. This topic is often connected to the very recent discovery of nanobubbles and micropancakes.

Experimentally, evidence has been found in favor of the existence of depletion layers. Experimental techniques, such as ellipsometry, X-ray reflectometry and neutron reflectometry are mainly used. Schwendel *et al.*, using neutron reflectometry, found a 2 nm depletion layer with a water density of only 9% of that of bulk water, although that could be caused by air trapped (nanobubbles) at the solid/water interface [8]. Again using neutron reflectometry, Doshi *et al*. found a reduced density layer of water in the direct vicinity of the hydrophobic substrate [5]. Furthermore, they found that the thickness of the depletion layer depended on whether the water contained dissolved gases. When ambient water was used to cover the hydrophobic substrate, the depletion layer had a thickness of 1.1 nm, while argon-gassed water showed a depletion layer of 0.2 nm. Also, studies made by Dammer *et al*. [7] and others [4] show that it is highly likely that there is a gas-enriched depletion layer at the direct vicinity of the hydrophobic substrate. However, there seems to be no consensus in the scientific community on whether gas-enriched depletion layers exist [6]. In general, the scientific publications show results in favor of a depletion layer, with a typical thickness that can range from 0.1 nm to approximately 1 nm [2,3,8,9].

On the other hand, experiments have also been made about which the authors have stated that the depletion layer is either unlikely to happen or that they are inconclusive about it. For example, Jensen *et al*., were unable to distinguish quantitatively the depletion layer of water on a hydrophobic surface using X-ray reflectometry, possibly due to low contrast between water and the substrate. They state that if the depletion layer does exist, the density of water at the depletion layer is approximately 90% of that of bulk water with a thickness of 0.1 nm [22]. Ellipsometry studies that have been published thus far generally belong to this area of opinion. Ellipsometry is a widely used tool for thin-film characterization. It is non-destructive, has a fast time resolution, and does not require delicate vacuum systems or low temperatures. Ellipsometry measures density variations at the solid/liquid interface. However, it has a poor lateral resolution, and cannot distinguish between nanobubbles, micropancakes, or gas-enriched depletion layers, just like X-ray reflectometry and neutron reflectometry. It is, however, suited for determining whether gas enrichment occurs at the solid/water interface. Castro *et al*., for example, have observed a layer of air of 0.5-1.0 nm in the depletion layer on a polystyrene layer of approximately 65 nm thick [10]. However, they did not see any air layer for a thicker layer of polystyrene of approximately 300 nm. Mao *et al*. investigated water on hydrophobic agents, they concluded that, if there were to be a layer of air in the depletion layer, it should be less than 0.1 nm thick [23]. Takata *et al*. stated that they found no evidence of a depletion layer [21]. The substrate they used was a hydrophobic alkylsilane in water.

It should be noted that X-ray reflectometry, neutron reflectometry, and ellipsometry cannot distinguish between gas-enriched depletion layers, or a high density of nanobubbles or micropancakes.

We will now focus shortly on these two forms of gaseous domains that can appear in a wetted surface: nanobubbles and micropancakes.

When pouring water in a glass beaker, one can clearly see the glass surface being wetted after the macroscopic bubbles have dissolved. However, when zoomed-in on a microscopic level, one would still observe miniscule gaseous domains at the solid/water interface. These microscopic gaseous domains exist in two main forms: nanobubbles [11,12,14-16] and micropancakes [13,17]. Nanobubbles were first reported in the literature by Parker *et al*. [14] when they were investigating the long-range hydrophobic attraction. This is the attraction between two hydrophobic plates when submerged in a liquid. The attractive force showed an increase in stepwise increments when they were brought together. They explained it by stating that nanobubbles smaller than 100 nm in size would fill the gap between the plates and cause an increase in the attractive force between them. The statement was a controversial one, because it was widely accepted that gaseous domains submerged in a liquid with dimensions measured in nanometers could not be stable, due to the gas inside the bubble rapidly dissolving into the surrounding liquid. This is the classical prediction by the Laplace equation [24]. Currently, the hydrophobic attraction is understood as capillary forces that arise when nanobubbles bridge the two hydrophobic plates.

A multitude of experimental techniques have been used to investigate surface nanobubbles, such as internal reflection infrared spectroscopy [25], rapid cryofixation [26], neutron reflectometry [16], and X-ray reflectometry [27]. Due to its excellent spatial resolution, unlike the methods mentioned before, the atomic force microscope (AFM) is usually preferred for surface nanobubble investigation [28,29].

In the experiments that have been done until recently, surface nanobubbles have been found with typical heights of 10-20 nm and widths of 50-100 nm with a spherically-capped shape. Micropancakes are much wider – several microns in diameter, but only 1-2 nm in height [6]. Nanobubbles have been found to be stable in water for days [30], outlasting classical lifetime predictions by at least 10 orders of magnitude. Why the classical prediction fails and nanobubbles are stable is not clearly understood and is a topic of debate.

The connection between (gas-enriched) depletion layers and nanobubbles and micropancakes is not always clear. There is a difference between nanobubbles and gas-enriched depletion layers in that they have different appearances. On the other hand, micropancakes are possibly related to the gas-enriched depletion layers [6]. It might be that all three types of gaseous domains are present on the surface when a hydrophobic substrate is submerged in water. Apart from the fact that there is no clear answer why nanobubbles are stable, there is also no consensus of the scientific community whether there is a gas-enriched depletion layer at all.

This thesis will focus on trying to answer the question following questions:

1) Does gas enrich the solid/water interface?
2) Is there a difference in enrichment between hydrophobic and hydrophilic surfaces?

We will use ellipsometry as our main experimental technique to qualitatively (and where possible, quantitatively) analyze whether gas layers form on the surface. The substrates that will be used are silicon with both a native oxide and thick oxide layer on top. The liquid used in our case is ultrapure Milli-Q water, with the option that it can be degassed or gas-saturated with a specific gas type. The silicon samples will also be hydrophobized to see the difference between hydrophilic and hydrophobic interfaces and whether gaseous domains form more easily at the latter. The effects of different gas types dissolved in water will also be investigated.

The conclusions of the previously performed ellipsometry by Mao *et al.* [23], Takata *et al.* [21], and Castro *et al.* [10], lean towards the statement that gaseous domains at the solid/water interface do not form, at least not consistently. This thesis will try to shed light on this topic, and provide answers where it possibly can. This will hopefully lead to a better understanding of the discrepancies reported in the literature.

Bibliography of Introduction

1. **Torigoe, A.D.** *How water meets a hydrophobic surface: Reluctantly and with fluctuations.* s.l. : University of Illinois, 2006.

2. *On the origin of the hydrophobic water gap: An X-ray reflectivity and MD simulation study.* **M. Mezger, F. Sedlmeier, D. Horinek, H. Reichert, D. Pontoni, H. Dosch.** 6735-6741, s.l. : Journal of the American Chemical Society, 2010, Vol. 132.

3. *How water meets a hydrophobic surface.* **A. Poynor, L. Hong, I.K. Robinson, S. Granick.** 266101, s.l. : PRL, 2006, Vol. 97.

4. *Interfacial water at hydrophobic and hydrophilic surfaces: Slip, viscosity, and diffusion.* **C. Sendner, D. Horinek, L. Bocquet, R.R. Netz.** 10768-10781, s.l. : Langmuir, 2009, Vol. 25.

5. **D.A. Doshi, E.B. Watkins, J.N. Israelachvili, J. Majewski.** 9458, s.l. : Proceedings of the National Academy of Science, 2005, Vol. 102.

6. *Nanobubbles and micropancakes: Gaseous domains on immersed substrates.* **J.R.T. Seddon, D. Lohse.** 133001, s.l. : Journal of Physics: Condensed Matter, 2011, Vol. 23.

7. *Gas enrichment at liquid-wall interfaces.* **S.M. Dammer, D. Lohse.** 206101, s.l. : PRL, 2006, Vol. 96.

8. *Interaction of water with self-assembled monolayers: Neutron reflectivity measurements of the water density in the interfaces region.* **D. Schwendel, T. Hayashi, R. Dahint, A. Pertsin, M. Grunze, R. Steitz, F. Schreiber.** 2284-2293, s.l. : Langmuir, 2003, Vol. 19.

9. *Water and ice in contact with octadecyl-trichlorosilane functionalized surfaces: A high resolution X-ray reflectivity study.* **M. Mezger, S. Schöder, H. Reichert, H. Schröder, J. Okasinski, V. Honkimäki, J. Ralston, J. Bilgram, R. Roth, H. Dosch.** 244705, s.l. : Journal of Chemical Physics, 2008, Vol. 128.

10. **L.B.R. Castro, A.T. Almeida, D.F.S. Petri.** 7610, s.l. : Langmuir, 2004, Vol. 20.

11. *Images of nanobubbles on hydrophobic surfaces and their interactinos.* **J.W.G. Tyrrell, P. Attard.** 176194, s.l. : PRL, 2001, Vol. 87.

12. *Nanobubble trouble on gold surfaces.* **M. Holmberg, A. Kühle, J. Garnaes, K.A. Morch, A. Boisen.** 10510-3, s.l. : Langmuir, 2003, Vol. 19.

13. *Nanoscale multiple gaseous layers on a hydrophobic surface.* **L. Zhang, X. Zhang, C. Fan, Y. Zhang, J. Hu.** 8860-4, s.l. : Lanmguir, 2009, Vol. 25.

14. *Bubbles, cavities and the long-ranged attraction between hydrophobic surfaces.* **J.L. Parker, P.M. Claesson, P. Attard.** 8468-8480, s.l. : Journal of Physical Chemistry, 1994, Vol. 98.

15. *Nanobubbles on solid surface imaged by atomic force microscopy.* **S. Lou, Z. Ouyang, Y. Zhang, X. Li, J. Hu, M. Li, F. Yang.** 2573-5, s.l. : Journal of Vacuum Science & Technology B, 2000, Vol. 18.

16. *Nanobubbles and their precurson layer at the interface of water against a hydrophobic substrate.* **R. Steitz, T. Gutberlet, T. Hauss, B. Klosgen, R. Krastev, S. Schemmel, A.C. Simonsen, G.H. Findenegg.** 2409-2418, s.l. : Langmuir, 2003, Vol. 19.

17. *Detection of novel gaseous states at the highly oriented pyrolytic graphite-water interface.* **X.H. Zhang, X. Zhang, J. Sun, Z. Zhang, G. Li, H. Fang, X. Xiao, X. Zeng, J. Hu.** 1778-83, s.l. : Langmuir, 2007, Vol. 23.

18. **Stillinger, F.H.** 141, s.l. : Journal of Solution Chemistry, 1973, Vol. 2.

19. **Barrat, J. L. and Bocquet, L.** 4671, s.l. : PRL, 1999, Vol. 82 (23).

20. **J. Janacek et al.** 8417-8429, s.l. : Langmuir, 2007, Vol. 23.

21. **Y. Takata, J.H.J. Cho, B.M. Law, M. Aratoni.** 1715, s.l. : Langmuir, 2006, Vol. 22.

22. **T.R. Jensen, M.O. Jensen, N. Reitzel, K. Balashev, G.H. Peters, K. Kjaer, T. Bjørnholm.** 086101-1, s.l. : PRL, 2003, Vol. 90 (8).

23. **M. Mao, J. Zhang, R.H. Yoon, W.A. Ducker.** 1843, s.l. : Langmuir, 2004, Vol. 20.

24. **V. Stuart, J. Craig.** 40-48, s.l. : Soft Matter, 2011, Vol. 7.

25. *Nanobubbles at the interface between water and a hydrophobic solid.* **X.H. Zhang, A. Quinn, W.A. Ducker.** 4756-4764, s.l. : Langmuir, 2008, Vol. 24.

26. *Rapid cryofixation/freeze fracture for the study of nanobubbles at solid-liquid interfaces.* **M. Switkes, J.W. Ruberti.** 4759, s.l. : Applied Physics Letters, 2004, Vol. 84.

27. *High-resolution in situ X-ray study of the hydrophobic gap at the water-octadecyl-trichlorosilane interface.* **M. Mezger, H. Reichert, S. Schoder, J. Okasinski, H. Schroder, H. Dosch, D. Palms, J. Ralston, V. Honkimaki.** 18401-18404, s.l. : PNAS USA, 2006, Vol. 103.

28. *Boundary slip and nanobubble study in micro/nanofluidics using atomic force microscopy .* **Y. Wang, B. Bhushan.** 29-66, s.l. : Soft Matter, 2010, Vol. 6.

29. **M. Mazumder, B. Bhushan.** 9184-9196, s.l. : Soft Matter, 2011, Vol. 7.

30. *Correlation between geometry and nanobubble distribution on HOPG surface.* **S. Yang, E.S. Kooij, B. Poelsema, D. Lohse, H.J.W. Zandvliet.** 64006, s.l. : Europhysics Letters, 2008, Vol. 81 .

2. Methodology

Following up on the goals of this thesis set in the Introduction, several theoretical and experimental aspects are mentioned in this chapter to give the reader an understanding of the research done by the author. Firstly, the sample preparation and measuring methods will be explained. Ellipsometry and our experimental setup will be discussed next, followed by the modeling methods used.

2.1 Sample preparation

Due to the scope of research that can be done on this area, there is a limited selection of base substrates to see whether gas-enriched depletion layers form. These are (i) silicon with native oxide (1-2 nm) and (ii) thermal oxide (277 nm) on top. Native silicon oxide is the oxide layer which forms on silicon when it is exposed to air, while thermal silicon oxide can be grown on silicon when it is heated in the presence of oxygen. The silicon oxide top layer has a highly hydrophilic property. However, this is only the case when it is freshly cleaned, because silicon is quickly contaminated with (organic) particles, which increases its hydrophobicity. When coated with a hydrophobic organic layer, it will exhibit a hydrophobic property.

2.1.1 Hydrophilic samples

The method used to acquire hydrophilic silicon samples is applicable for both native and thick oxide silicon. Silicon samples are first diced in approximately 15×15 mm-sized squares with a thickness of 0.5 mm. After this process, the samples are put in a glass beaker and cleaned with a piranha solution (a mixture of H_2SO_4 and H_2O_2 in a 3:1 volume ratio). This treatment will remove organic material from the surface and the sample will be ready for measurement after it is rinsed with Milli-Q water several times.

2.1.2 Hydrophobic samples

The hydrophobization of silicon samples is complex and requires skillful handling of samples and tools. The chemicals used in this case are: PFDTS (1H,1H,2H,2H-perfluorodecyltrichlorosilane), FOTS (trichloro(1H,1H,2H,2H-perfluorooctyl)silane), and silicone oil. Detailed information about these chemicals can be read in section 5.1 of the Appendix. Two primary hydrophobization methods have been used: vapor coating (for PFDTS, FOTS) and silicone oil coating. The cleaning procedure before the coating is the same for both methods: silicon wafers are first cleaned in an ultrasonic bath in a beaker with a mixture of deionized water, isopropyl alcohol, and acetone in a 1:1:1 volume ratio for about 15 minutes. Then, the beaker is again placed in the ultrasonic bath for about 15 minutes with the liquid replaced by isopropyl alcohol. The samples are then placed in the O_2 plasma cleaner for 15 minutes which will remove any organic material on the surface. After the samples are thoroughly cleaned, they are ready for hydrophobization.

2.1.3 Vapor coating

Vapor coating with FOTS or PFDTS requires a chamber with several attachments that can be put under low pressure, a schematic overview of which can be seen in Figure 1**.**

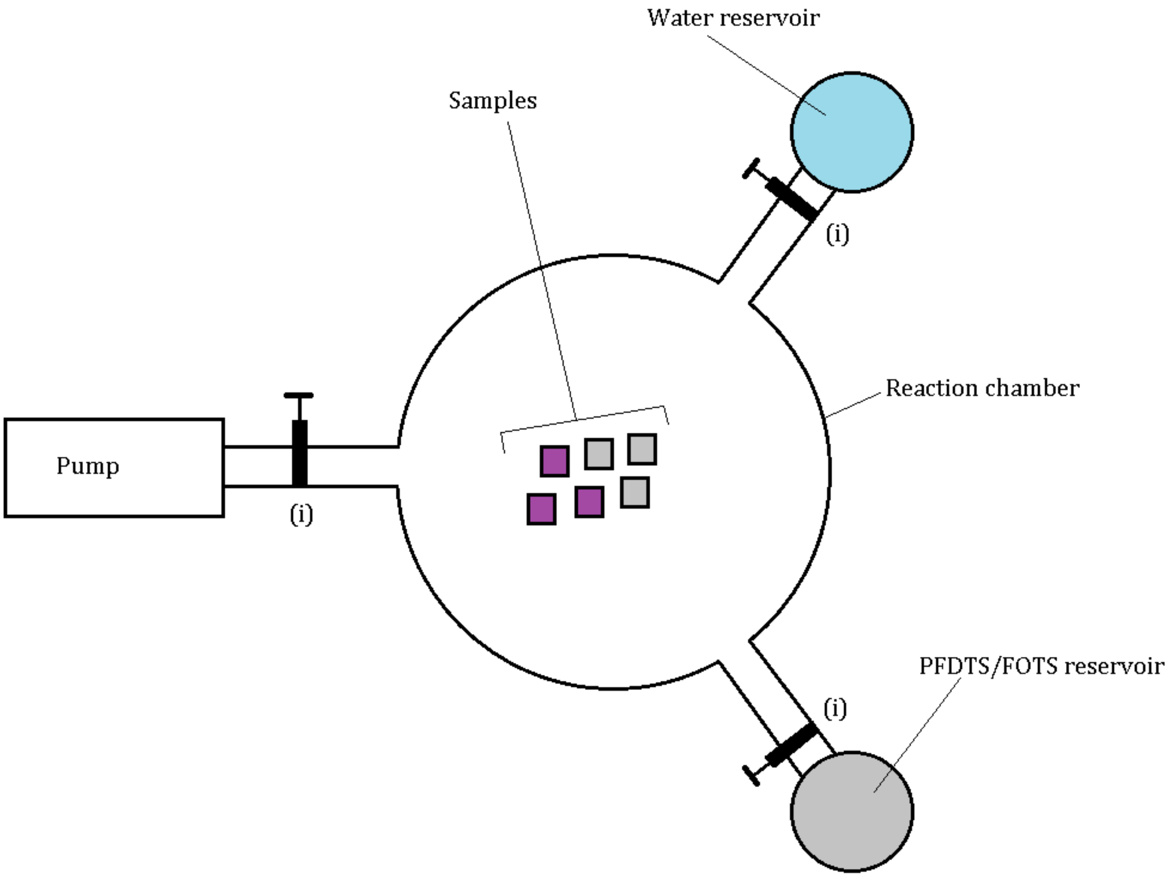

Figure 1. Schematic top view of the reaction chamber used to coat samples with PFDTS and FOTS. The valves are denoted by (i).

The samples are put in the main reaction chamber, which is put under low pressure (usually around 5×10^{-2} mbar) with a pump. There are two attachments with a valve to the main reaction chamber, one contains deionized water, while the other contains liquid FOTS /PFDTS. The valve connecting to the FOTS/PFDTS reservoir is opened first, after which the FOTS/PFDTS will evaporate immediately, filling the main reaction chamber while the valve connecting to the pump is closed. After waiting for several minutes, the valve connecting to the FOTS/PFDTS reservoir is closed. Hereafter, the valve connecting to the deionized water reservoir is opened for a few seconds and closed again. This leads to water coming in the reaction chamber and reacting with the chemical at the substrate surface, as can be seen in section 5.1.1 and 5.1.2 of the Appendix. After waiting for several minutes, the pressure in the chamber is equilibrated with the ambient pressure by turning off the pump and allowing air to come in via a vent. The hood of the reaction chamber is then taken off and the samples are extracted. They are put in an oven at 120 °C for one hour in a low pressure environment to prevent contamination. The samples are then ready for measurement.

2.1.4 Silicone oil coating

After the silicon samples are cleaned in the plasma chamber, silicone oil is applied immediately on its surfaces, covering it completely. Then the samples are put in a UV chamber where they are irradiated for 10 hours. This is the step where the silicone oil molecules are broken down and chemically bind with the substrate interface, as explained in section 5.1.3. Hereafter, the samples are put in a beaker in a sample holder in a mixture of iso-octane and acetone in a 1:1 volume ratio while stirring. This step washes off the oil and takes about 30 minutes. Then the liquid is replaced by acetone and is followed by another 30 minutes stirring period. The samples are then rinsed with deionized water and put in an oven at 120 °C for one hour in a vacuum environment to prevent contamination. This is the final step and the samples are ready for measurement.

2.2 Contact angle measurements

Differentiating between hydrophilic and hydrophobic surfaces is an important aspect in this thesis. One of the ways to do this is to use an optical contact angle measurement. Static contact angle measurements usually are sufficient for this purpose.

2.2.1 Static contact angle

Measuring the static optical contact angle will provide information about the hydrophobicity of the surface. If the static contact angle exceeds 90°, the surface is classified as hydrophobic. If it is below 90°, it will be classified as hydrophilic. The measurement procedure with the goniometer is as follows: the sample is set on a flat surface where it is in view of the camera. A syringe infuses a Milli-Q water drop of 1 µL on the surface, the curvature of the droplet is then analyzed by the program. The angle between the droplet surface and the flat surface is drawn and calculated, as it can be seen in Figure 2.

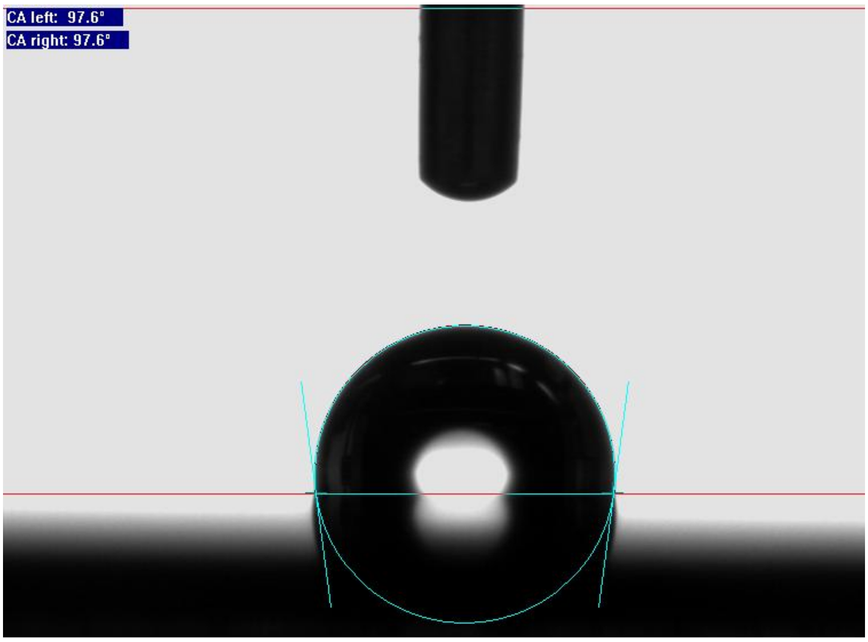

Figure 2. Static contact angle measurement of a water droplet on a PFDTS-coated silicon oxide surface.

2.3 Ellipsometry

The main measuring technique used in this thesis to research potential gas-saturated layers forming on the solid/water interface, is ellipsometry.

Ellipsometry has been known since 1887, when Drude formalized its equations [1]. Ellipsometry measurements were initially conducted at a single wavelength of light and were time consuming. In the late 20th century, the process became automatized [2] and it quickly grew to being a common method for studying thin film layers. The following section briefly discusses the basics of ellipsometry.

2.3.1 Basics of ellipsometry

Light is a propagating electromagnetic wave traveling at light speed c. It has an oscillating transverse electric and magnetic field, but, for the purposes of this paper, it is sufficient to look only at the oscillating electric field.

When light is emitted from a regular light source, like a lamp, its electric fields orient randomly in all possible directions perpendicular to the propagation vector [3]. This is referred to as unpolarized light. Next to this, there are several forms of polarization of light: linear, circular, and elliptical. These can be seen in Figure 3.

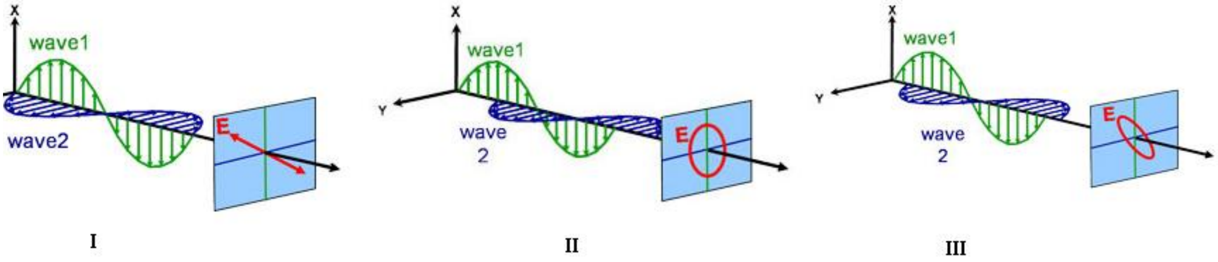

Figure 3. Polarization of light in three different forms: linear (I), circular (II), and elliptical (III). Wave 1 and 2 indicate the electric field oscillations of the s and p components of the electrical field [7].

When the electrical field is oscillating perpendicularly in one plane, it is linearly polarized. When the endpoint of the electrical field intensity precesses along a circular and elliptical trajectory, it is referred to as circular and elliptical polarized light, respectively. The time needed for one precession is defined as $\frac{2\pi}{\omega}$, where ω is the angular frequency of light [4].

2.3.2 Parameterization

The polarization of the electrical waves of light is parameterized into the s and p polarizations. The s and p polarization refer to the component of the electrical field perpendicular and parallel to the plane of incidence, respectively. Light as seen from a viewpoint where it is propagating directly to the reader is illustrated in Figure 4, which will be further discussed below.

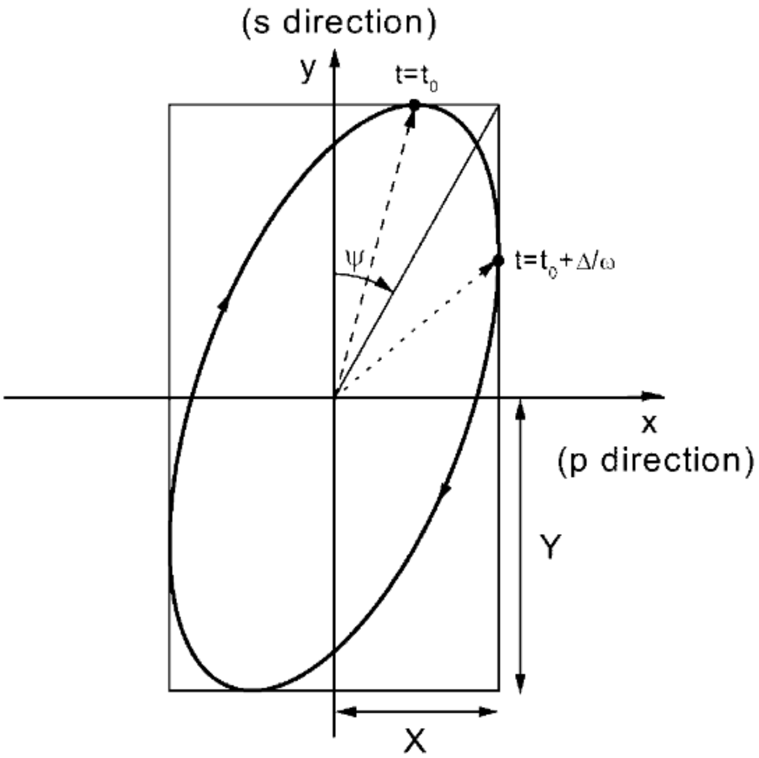

Figure 4. The precession of the electrical field of a light wave as seen from the direction of its propagation [4].

When light with a known polarization is reflected off a surface, its polarization will change as can be seen in Figure 5. The interpretation of Δ and Ψ is discussed later on in this section.

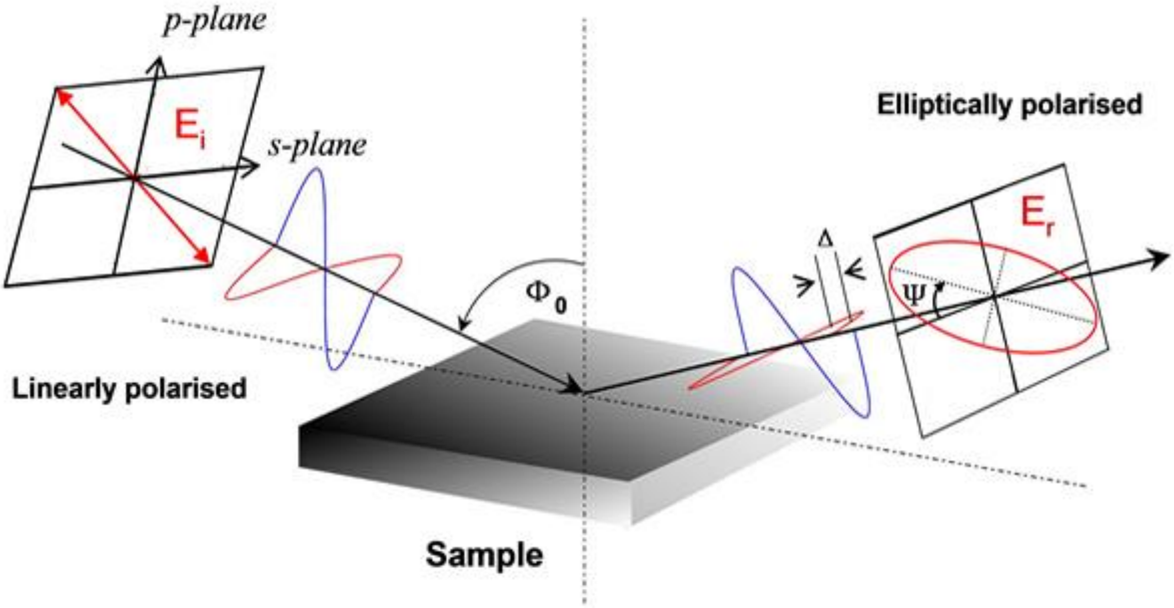

Figure 5. Linearly polarized light which reflects off a surface acquires a polarization change. In this case the reflected light is elliptically polarized. Φ_0 denotes the angle of incidence [5].

This change in polarization is determined for example by the angle of incidence, and the optical properties of the surface, such as film thickness, roughness, dielectric constants, etc. The change in polarization is expressed by two main parameters: Ψ and Δ. The parameter Ψ refers to the ratio of reflection coefficients of the s and p polarized light waves:

$$tan(\Psi) = \frac{|r_p|}{|r_s|}.$$

The parameter Δ refers to the phase difference between the s and p polarized light waves:

$$\Delta = \delta_p - \delta_s$$

The δ_p and δ_s denote the phase change acquired by the s and p polarized light waves respectively upon reflection from the surface. In ellipsometry, the complex reflectance ratio [6] is measured, which is the ratio between the s and p reflection coefficients, and is given commonly expressed as:

$$\rho = \frac{r_p}{r_s} = tan(\Psi)\, e^{i\Delta}$$

It is for this reason that ellipsometry is relatively insensitive to intensity fluctuations and requires no reference beam. Furthermore, it is a highly accurate and reproducible measuring method, with a thickness sensitivity that can reach ~0.1 Å [6].

2.3.3 Modeling

Modeling is an important aspect of ellipsometry as it provides a physical interpretation of the measured data. A model is constructed from Fresnel equations, which describe the properties of light when it passes through materials of different refractive indices n and extinction coefficients k. After having acquired the predicted response for Ψ and Δ, it is compared to the measured signal. With each iteration, fit parameters are adjusted until the MSE (mean square error) between the model and real data has arrived at a minimum. This procedure can be seen in Figure 6.

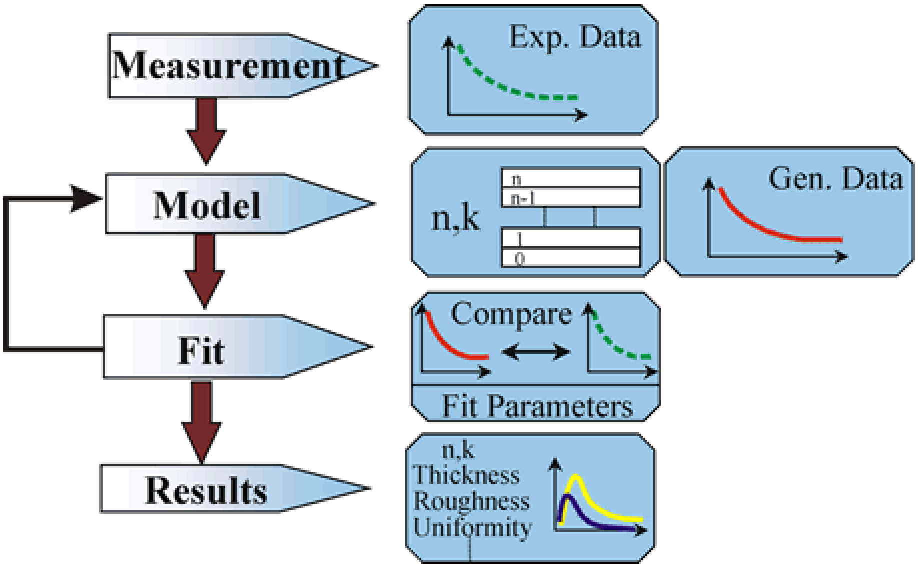

Figure 6. Modeling procedure for ellipsometry data [7].

An important remark would be that one can adjust any parameter in a model and still match the ellipsometry data nicely, while it would not have any physical meaning. This is why it is important to keep the number of fit parameters as low as possible.

2.3.4 Advantages and disadvantages

The main advantages of ellipsometry are that it is non-destructive, highly accurate. However, ellipsometry has a very low spatial resolution. It is an indirect method because of the necessity of an optical model for data analysis. Furthermore, ellipsometry data have to be supported by other characterization methods such as Atomic Force Microscopy (AFM), to gain a proper understanding of the topology of the surface that is under investigation [6].

2.3.5 Further reading

For the reader who is interested in reading an in-depth theoretical background on ellipsometry, books by H. Fujiwara [6], H. G. Tompkins [3,4] are good choices.

2.4 Experimental setup

Ellipsometry experiments are usually done where the sample under investigation is held in an air ambient. For the purposes of this thesis, samples must be held under water during measurement. To meet this requirement, a liquid cell which can be filled with water, is used with glass windows at a fixed angle. The ellipsometer itself is a J.A. Woollam model. A schematic view of the experimental setup can be seen in Figure 7.

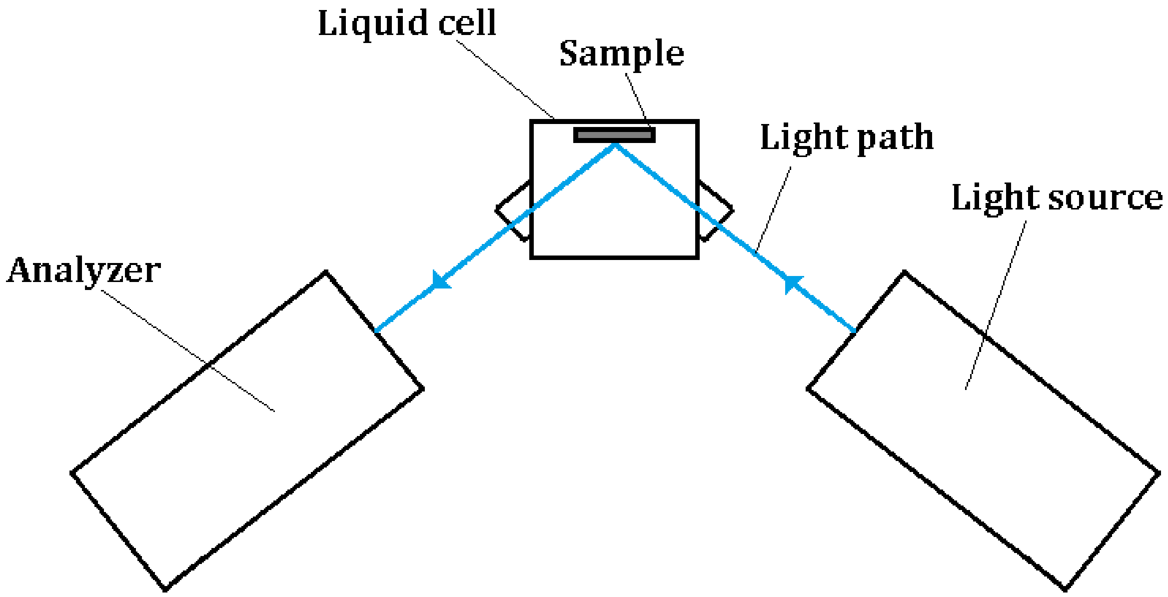

Figure 7. Schematic top view of the ellipsometry setup with the water-filled liquid cell mounted.

When measuring the effect of a degassed or gas-saturated (with an arbitrary gas type) water ambient, the sample is submerged in water and light from the source reflects off it. The reader should note that the system in the liquid cell is not closed, thus when the gas type dissolved in the liquid is not equal to that of air, diffusion will take place and is noticeable after typically 30 minutes with the oximeter (this in turn depends on how long the diffusion length is).

2.4.1 Spectroscopic scans and dynamic scans with the ellipsometer

The experiments done with the ellipsometer are done in two ways: spectroscopic scans and dynamic scans. The methods of performing each type of scan will be discussed below.

Before any measurement is done, there is a standard procedure of degassing the entire liquid cell with sample mounted, and Milli-Q water filling it. The liquid cell is placed in an evacuation chamber, which is connected to a membrane pump. The chamber is then depressurized, this is done to remove any gaseous domains on the surface of the substrate. The degassing procedure inside the evacuation chamber lowers the O_2 concentration in water to less than 1% of that of its saturation value. It is assumed the other gases naturally present in water will also be largely removed, even though we only recorded the O_2 saturation. While degassing the water in the liquid cell, the temperature drops as a result of water evaporating, that is why a heater is held underneath the chamber to keep the water in the liquid cell at room temperature. This step takes approximately 25 minutes, after which the entire liquid cell is removed from the evacuation chamber, and mounted for measurement. The first scan is interpreted as a control measurement.

Gas-saturated water is prepared by degassing water in an evacuation chamber for approximately 15 minutes, whilst stirring and at room temperature. Hereafter, a saturator is connected to a gas source (for example, N_2) and gas is bubbled through the water for 25 minutes.

The preparation of gas-saturated water is then complete and can be used to change the water ambient in the liquid cell explained in 2.4.2.

2.4.2 Spectroscopic scans

To negate the effects of diffusion, spectroscopic scans would have to take less than 30 minutes to complete. In our case spectroscopic scans usually take approximately 25 minutes, with increments in the photon energy of 0.05 eV. One could measure for a shorter period of time, but the energy resolution would deteriorate.

The reader should be reminded that the ellipsometer data is gathered from a patch of light of several mm^2 that is reflected off the sample. To compare the effects of gas-saturated water compared to degassed water, one would have to repeatedly change the water ambient between degassed and gas-saturated water. The different ways to cycle between gas-saturated and degassed water ambients is explained in the following:

- The first method is simply to empty the liquid cell of the bulk of its water with a syringe, after which a freshly prepared amount of water is poured in the cell. For example, if the liquid cell has degassed water, after the measurement it is removed and replaced with gas-saturated water, then with gas-saturated water, etc. One clear disadvantage of this method is that the sample becomes dry when removing the water from the liquid cell, and air may get trapped to form nanobubbles at the surface. What would then be measured is not any surface-induced gas on the substrate surface, so the results taken with this method could be misleading. It is also not straightforward to have a consistent way of pouring water in the liquid cell.

- The second filling method is by exchanging the water while it is mounted. After measurement, gas-saturated or degassed water is led through a tube which ends close to the bottom of the liquid cell. The excess water is then drained by a tube mounted at the top of the liquid cell, which tunnels the water to the syringes connected to a syringe pump. This cycle is maintained until the end of the series of measurements. The volume of water which is being replaced is 200 ml, which is enough to replace the water in the liquid cell approximately 7 times. A zoom-in picture of the liquid cell whilst using this method, can be seen in Figure 8. This method provides proper exchange of the liquid without rewetting the sample, and thus prevents any air pockets getting trapped at the surface. However, local diffusion of gas and its adsorption on the surface may be too slow during the measurement. Photon energy increments are in this case also 0.05 eV.

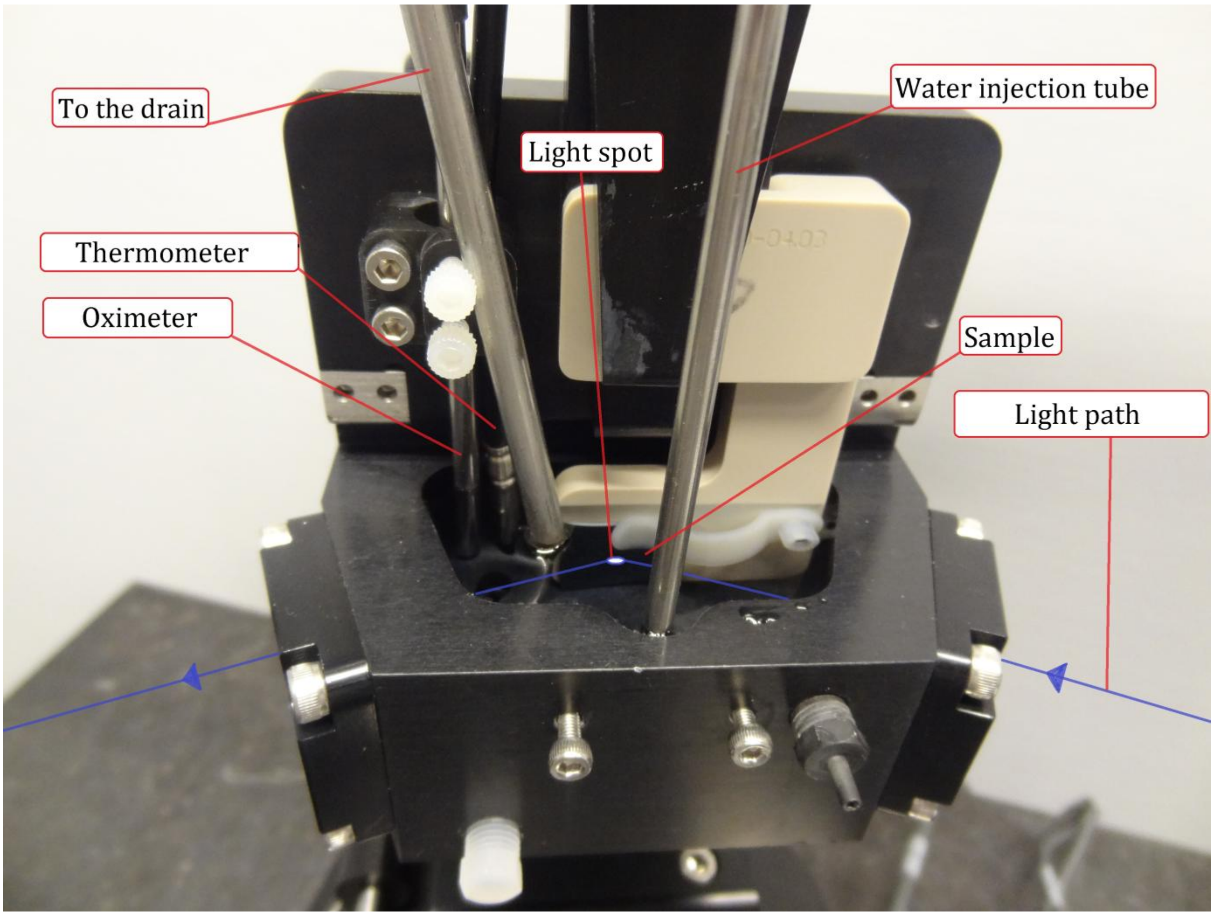

Figure 8. Photo taken of the liquid cell after measurement with the exchange method.

- The third method relies on injecting the liquid directly on the light spot where data is gathered, as it can be seen in Figure 9. It should be noted that the sample together with the light spot is under water during measurement. The blue water beam at the end of the water injection tube is only visually representing the water exiting the tube.

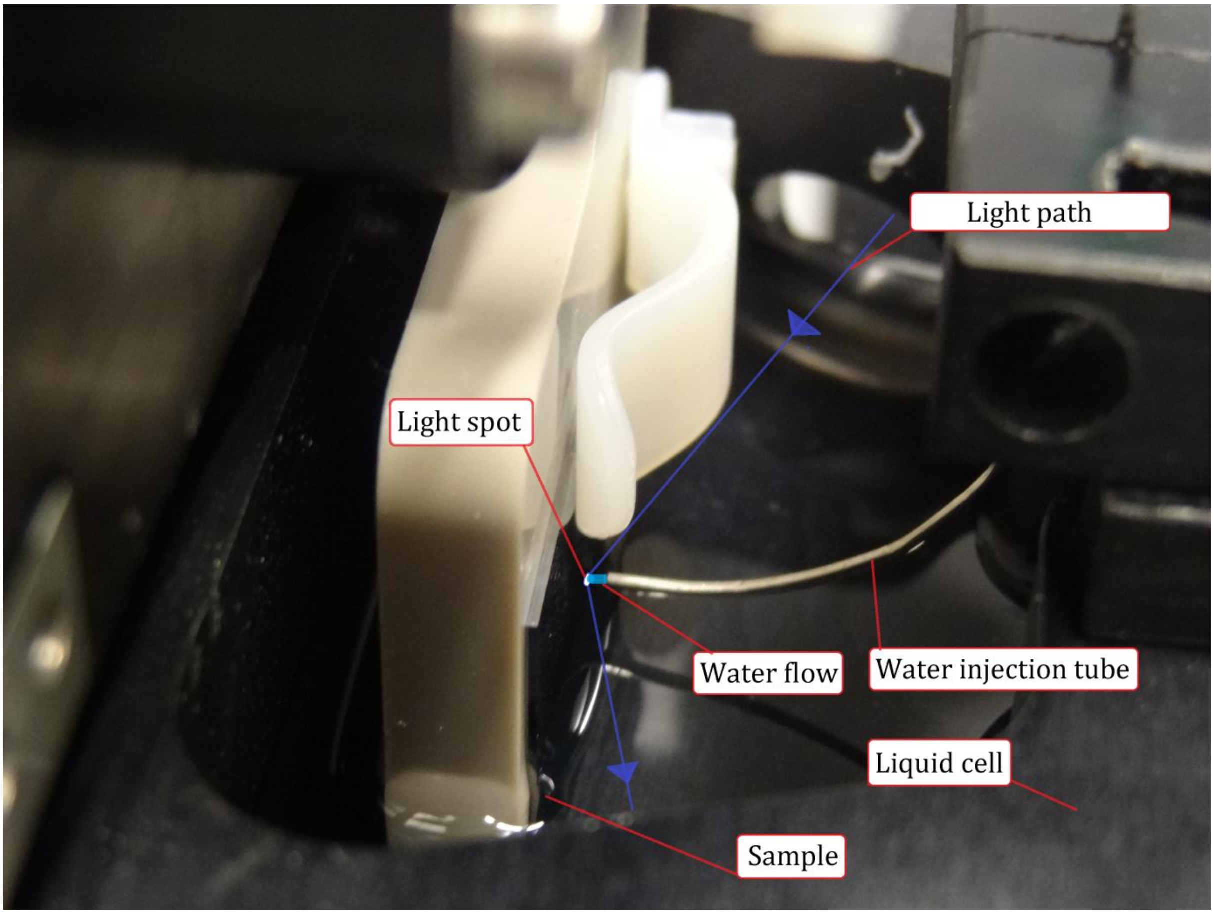

Figure 9. Photo taken of the liquid cell with the water injection tube mounted. Note that the liquid cell is dry in this case.

During the entire period of each measurement, water is injected onto the sample. This would mean that the local environment near the surface becomes changed instantly and one would not have to rely on diffusion of gas. It also possible that any gaseous layer that may be forming at the solid/water interface could be removed by the pressure of the water jet. At each measuring cycle, the water reservoir which feeds the injection tube is changed. Due to the limited amount of water in the syringe (100 mL), which is connected to the syringe pump, the measuring time is restricted to about 12 minutes. This in turn means that the increments made in the photon energy should be 0.1 eV.

Each series of spectroscopic measurements is characterized by the fact that water starts out as degassed, after which it is gassed, degassed, gassed, etc. At each degassed or gassed state, a spectroscopic measurement is made. Table 1, which summarizes the methods used for the spectroscopic scans, is shown below.

Method	Properties	Increments in photon energy (eV)
Pouring	Sample is being rewetted. Highly probable that air is being trapped, interfering with data.	0.05
Water exchange	Sample is kept wet. Proper exchange of water with different amounts of dissolved gases.	0.05
Water injection	Sample is kept wet. Diffusion parameter effectively negated. Gaseous layers that may have been forming could be removed by the pressure of the jet.	0.1

Table 1. Properties of each measuring method listed together with the energy increments (which indicates energy resolution) made during measurement.

2.4.3 Dynamic scans

Dynamic scans, which are series of spectroscopic scans, may take a lot longer to include the effect of diffusion, and hence possible gas adsorption, in the ellipsometer signal. Usually they take longer than 100 minutes. The experimental procedure is the same as explained under section 2.4.1: the liquid cell with sample placed and degassed water inside, is mounted on the ellipsometer for measurement. This is the main starting point for all dynamic scans.

From this point on, if the measurement has to be done in a degassed water ambient, the water is not exchanged with another water type, so air will diffuse in the water and onto the sample, which can then be related to the difference in ellipsometer signal measured.

For initial N_2-saturated and He-saturated water ambients, the degassed water is simply exchanged by N_2-saturated and He-saturated water, and the measurements start immediately after the exchange process.

2.4.4 Sample cleaning

Due to the limited amount of samples compared to the larger amount of experiments done, it is important to consistently clean samples. Hydrophobic and hydrophilic samples have their own method of doing so.

- After each measurement, hydrophobic samples undergo cleaning in an ultrasonic bath in a hexane solution for 15 minutes. Here after, the hexane is replaced by acetone and the process is repeated. Then, the samples are rinsed in Milli-Q water 5 times, after which the cleaning procedure is completed. The samples are stored in air.
- Hydrophilic samples are cleaned using piranha, after which they are rinsed 10 times in Milli-Q water. This completes the cleaning procedure and the samples are stored in air.

2.5 Diffusion of gas in water

When doing dynamic scans, the ellipsometer signal is measured over time. The reason why dynamic scans are made is that gas diffusing from air to the submerged sample can be adsorbed on its surface. This in turn can change the signal detected by the ellipsometer over time. The *calculated gas saturation profile can be used to fit and subsequently plot the change in ellipsometer signal against the gas concentration in the BET model.*

Diffusion of gas in water in the vertical direction is similar to heat diffusion. Fick's second law of diffusion will be used in our case to relate the concentration of gas near the light spot on the sample to the time, as can be seen in Figure 10.

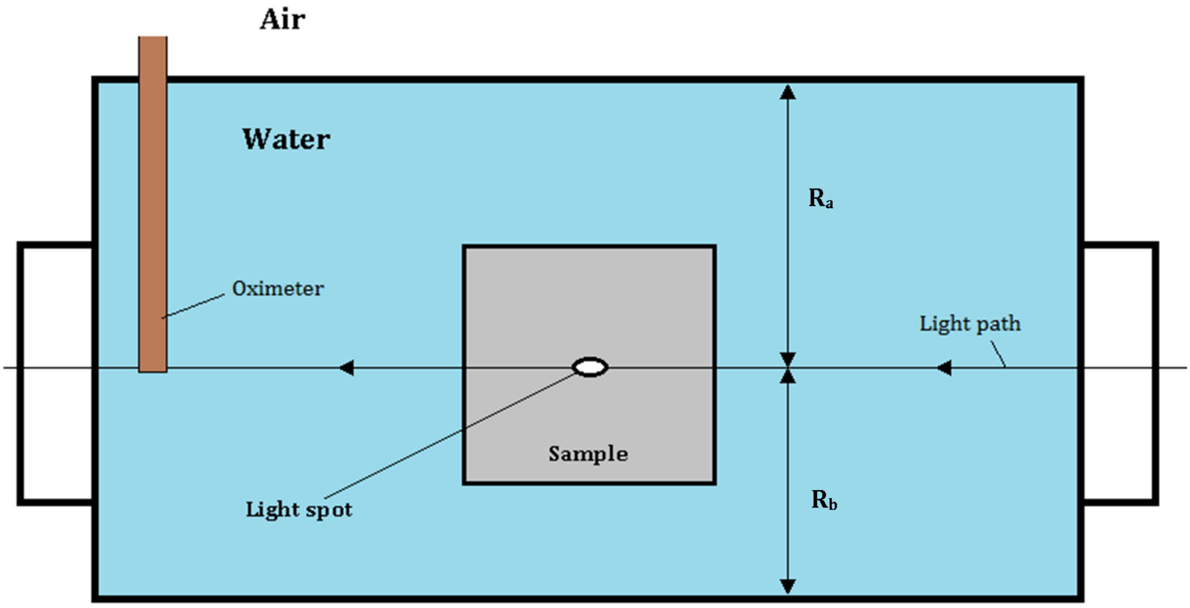

Figure 10. Schematic front view of the liquid cell during measurement.

For future calculations, we define a location variable inside the liquid cell R as:

$$R = \frac{R_b}{R_a + R_b}$$

The main equation used to find an expression for the concentration of gas *u(x,t)* (mol/m^3) as a function of depth *x* (m) and time *t* (min) is given below:

$$\frac{du}{dt} = D\frac{d^2u}{dt^2}$$

D is the diffusion constant of a type of gas in water (m^2/s), it can range from 1 to 7×10^{-9} m^2/s depending on the molar volume of the type of gas [8]. High molar volume gas types (such as CH_3Br) show a diffusion constant between 1 and 2×10^{-9} m^2/s at 25 °C. Low molar volume gas types (such as He) show a diffusion constant higher than 3×10^{-9} m^2/s. In our case, diffusion constants of O_2 and N_2 are similar: 2×10^{-9} and 1.9×10^{-9} m^2/s at 25°C, respectively [9]. The steady state solution for the concentration profile $u_s(x)$ is a constant u_{out}, which is the saturation concentration of any arbitrary type of gas in water.

The steady state solution will be used in the time dependent solution *u(x,t)* in the following way:

$$u(x,t) = u_s(x) + v(x,t)$$

v(x,t) represents the difference between the time dependent solution and the steady state solution. When identifying the boundary conditions for *v(x,t),* one can arrive at the following:

$$v(0,t) = \frac{dv(L,t)}{dx} = 0$$

The depth x ranges from 0 to L, with 0 being the water/air interface at the top and L the bottom of the liquid cell. After separation of variables and solving the time and space dependent differential equations separately, we arrive at the following:

$$u(x,t) = u_{out} + \sum_{n=1}^{\infty} b_n e^{Dt\left(\left(\frac{2n-1}{2}\right)\frac{\pi}{L}\right)^2} \sin\left(\left(\frac{2n-1}{2}\right)\frac{\pi}{L}x\right)$$

$$b_n = \frac{2}{L}\int_0^L v(x,0)\sin\left(\left(\frac{2n-1}{2}\right)\frac{\pi}{L}x\right)dx = \left(\frac{4}{\pi}\right)\frac{u_0 - u_{out}}{2n-1}$$

The concentration profile *u(x,t)* is a summation which is dependent on the amount of Fourier coefficients n (which, for computational reasons will be finite) and coefficient b_n. The starting concentration of gas in the liquid cell is not zero, but a value u_0.

2.6 BET-model

The BET-model is often used for explaining the adsorption of gas molecules at a solid surface. The BET equation is as follows:

$$\frac{p}{v(p_0 - p)} = \frac{1}{v_m c} + \frac{c-1}{v_m}\frac{p}{p_0}$$

Where p is the pressure (N/m^2) of the gas, p_0 is the saturation pressure of the gas, v is the volume of the gas adsorbate on the surface, v_m is the volume of one monolayer of gas adsorbate, and c is the BET constant which is related to the energy of adsorption and liquefaction of the gas [13]. This model can be used to see if our data can be fitted with the BET theory, and whether the gas pressure plays a role in the thickness of a possible gas adsorbate layer.

2.7 Model predictions

When interpreting ellipsometry data, it is useful to compare with models where all parameters are set constant, except for one, which is slightly varied. The effect of the change in this parameter can be then be studied. This could provide meaningful qualitative insight on the research topic. Model predictions are split up into two parts. In the first part, the effect of dissolved air in water will be compared to that of a degassed state. In the second part, the modeling with the WVASE software will be done.

2.7.1 Effect of dissolved air in water

The effect of air dissolving in water could be affecting ellipsometry data by changing the refractive index of water. To investigate if such an effect is playing a significant role in our system, the Lorentz-Lorenz equation is used which relates the polarizability of a material to its refractive index. Table 2 contains the necessary information to calculate the change in refractive index of pure, degassed water as it is gassed with air in a steady state solution.

Molecule type	**Polarizability volume (Å^3) [10,11]**	**Amount of particles in steady state 1 mol water solution (mol) [12]**
H_2O	1.45	1
N_2	1.76	1.1×10^{-5}
O_2	1.56	2.34×10^{-5}
CO_2	2.56	6.12×10^{-4}

Table 2. Polarizability volumes (Å^3) and amount of particles of gas dissolved (mol) in 1 mol water at the steady state solution given for several molecule types.

The polarizability volume can easily be converted to the molecular polarizability in SI units by multiplying with $1/4\pi\varepsilon_0$. The total polarizability is given by the following formula:

$$\alpha_{tot} = \frac{N_{H_2O}\alpha_{H_2O} + N_{CO_2}\alpha_{CO_2} + N_{N_2}\alpha_{N_2} + N_{O_2}\alpha_{O_2}}{N_{H_2O}}$$

When comparing the total polarizability of air gassed water to that of pure, degassed water (α_{H_2O}), it has increased with 0.047%.

This change in polarizability would translate to a maximum difference in refractive index of less than 3.5×10^{-8} % compared to the pure water ambient. This is calculated with the Lorentz-Lorenz equation:

$$\frac{n^2-1}{n^2+2} = \frac{4\pi}{3}N\alpha$$

With n being the refractive index, N the number of molecules in the given volume, and α the mean polarizability in Cm^2V^{-1}.

Thus it can be argued that the change in refractive index due to dissolved gases would not be influencing the ellipsometer signal, because the effect will be dominated by signal noise.

2.7.2 Modeling with WVASE software

After an ellipsometry measurement, the data is modeled by several layers with different optical properties. In general, it is important to adhere to the simplest of models with the least amount of parameters. The model generally used in this thesis can be seen in Figure 11.

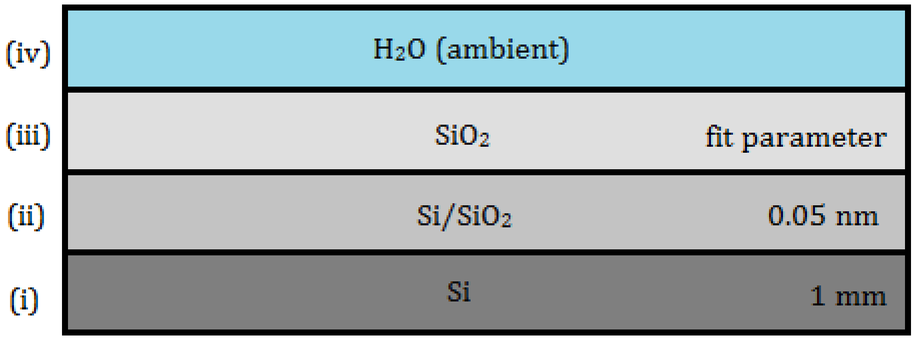

Figure 11. Schematic overview of the most common model used in this thesis. The first layer (i) is the Si substrate with a thickness of 1 mm. (ii) is the mixing layer between Si and SiO_2, which is always set to 0.05 nm. (iii) is the SiO_2 layer, which will include the following: SiO_2, organic hydrophobic coating, gas adsorbates, or even contaminations. The thickness of this layer is the fitting parameter. The final layer (iv) is the water ambient, the temperature of which is 21 ± 1°C, and can be assumed constant.

In this case, the only fit parameter is the SiO_2 thickness. It was a deliberate choice not to include extra layers for the hydrophobic organic coating and potential gas-enriched depletion layers to keep the number of parameters at a minimum. The thickness of the solid substrate (i.e. SiO_2 and, if used, the hydrophobic organic coating) is assumed to be constant. The change in the fitted thickness of the SiO_2 layer could then be attributed to gaseous bodies forming at the solid/water interface (note that this method cannot distinguish between nanobubbles or gas adsorbates, as explained before). One could use the equation for the optical thickness [14] to relate the real average thickness of a layer d_{real}, to its refractive index n and fitted thickness d_{model}:

$$d_{real} = n \cdot d_{model}$$

The problem when calculating with this method is that d_{real} and n are unknown to begin with. We would then increase the number of parameters for our fit, which is undesirable. Even if we would only use the SiO_2 thickness as a fitting parameter, this would not defeat the purpose of this thesis. After all, it is the qualitative differences in ellipsometer signals between different samples and conditions we are looking for.

2.7.3 Modeling with WVASE software prior to measurement

The system under investigation has a number of variables that have an effect on our ellipsometer signal. These are for example: the temperature, the SiO_2 layer thickness, changes in refractive index of the layer under investigation, whether or not a gas layer or a void exists, etc. It is worthwhile to slightly change any of these parameter values, while keeping the other parameters constant, this way, the effect of the change in each parameter value can be related to the change in ellipsometer signal. Therefore, during data analysis, the change in ellipsometer signal can then be attributed to changes in parameter values that were modeled beforehand. Due to the extensiveness of the amount of parameters used in the modeling, this part has been moved to section 5.2 of the Appendix.

Bibliography of Methodology

1. *Ueber die Gesetze der Reflexion.* **Drude, P.** 12, s.l. : Annalen der Physik, 1889, Vol. 268.

2. **D.E. Aspnes, A.A. Studna.** 220-228, s.l. : Applied Optics, 1975, Vol. 14.

3. **Tompkins, H.G.** *A User's Guide to Ellipsometry.* 1993.

4. **H.G. Tompkins, E.A. Irene.** *Handbook of ellipsometry.* 2005.

5. University of Dublin. [Online] http://www.tcd.ie/Physics/Surfaces/ellipsometry2.php.

6. **Fujiwara, H.** *Spectroscopic ellipsometry principles and applications.* s.l. : John Wiley & Sons, 2007.

7. [Online] J.A. Woollam Co., Inc. http://www.jawoollam.com/tutorial_5.html.

8. *Uncertainties in the Molecular Diffusion Coefficient of Gases in Water for Use in the Estimation of Air-Sea Exchange.* **D.B. King, W.J. De Bruyn, M. Zheng, E.S. Saltzman.** s.l. : University of Miami, 1995.

9. **Cussler, E.L.** *Diffusion - mass transfer in fluid systems.* Cambridge : Cambridge University Press, 1984.

10. *Molecular and Atomic Polarizabilities: Thole's Model Revisited.* **P.T. Duijnen, M. Swart.** 14, s.l. : Journal of Physical Chemistry A, 1998, Vol. 102.

11. **Pauling, L.** *General Chemistry.* s.l. : Courier Dover Publications, 1988.

12. **Sander, Rolf.** Henry's Law. [Online] http://www.henrys-law.org/.

13. **S. Brunauer, P.H. Emmett, E. Teller.** 309, s.l. : Journal of the Americal Chemical Society, 1938, Vol. 60.

14. *The Optical Measurement of Depth.* **Galbraith, W.** 3, s.l. : Journal of Microscopical Science, 1955, Vol. 96 .

3. Results and discussion

The analyzed data gathered in the course of this thesis, together with the discussion thereof, will be summed up in this section. Firstly, the contact angle data on the samples that were prepared will be presented. Secondly, we will look at the results obtained by the dynamic scans and how to interpret them with the oxygen diffusion data and the BET theory. Further on in this chapter, recommendations have been proposed for future experiments to gain a more thorough understanding on this subject.

3.1 Contact angle measurements on prepared samples

Two main substrates were investigated in this thesis: silicon with thermal oxide (277 nm), and silicon with native oxide (1-2 nm) on top. Due to the time limitations, our attention was focused more heavily on the thermal oxide silicon than the native oxide samples. Both substrate types are by themselves hydrophilic due of the –OH terminated groups at the interface. The static contact angle of freshly etched silicon oxide (i.e. non-coated) samples typically has values of 5°.

To investigate whether hydrophobicity has any effect on the ellipsometry signal, it is essentially to keep the contact angle of the sample under investigation constant to reduce the number of parameters in our system. Therefore, we tested whether the static contact angle for different types of hydrophobic coatings change after they are wetted for a period much longer than our measurement time. Further information on the hydrophobization of the sample can be found in section 2.1 of Methodology. We started by wetting the hydrophobized silicon oxide (both native and thermal oxide) in water for 91 hours. The average static contact angle was measured before and after wetting for different samples. The RMS roughness for silicone oil coated and uncoated samples were measured with the AFM. These results are provided by Table 3.

Coating type	Average static contact angle before H_2O wetting (°)	Average static contact angle after H_2O wetting (°)	RMS roughness (nm)
FOTS	105.0 ± 1.5	103.6 ± 1.5	Not measured
Silicone oil	96.9 ± 1.5	97.7 ± 1.5	0.71
PFDTS	95.2 ± 1.5	90.1 ± 1.5	Not measured
No coating	5.0 ± 1.5	Not measured[1]	0.23

Table 3. The average static contact angle before and after 91 hours of wetting with H_2O for different coating types. The RMS roughness is also included.

In the second case, the effects of wetting in the IPA/acetone mixture was tested, as these samples undergo cleaning with these chemicals. The total wetting time was 5 hours, and the results can be seen in Table 4.

Coating type	Average static contact angle before IPA/acetone cleaning (°)	Average static contact angle after IPA/acetone cleaning (°)
FOTS	105.0 ± 1.5	96.0 ± 2.0
Silicone oil	96.9 ± 1.5	96.3 ± 1.5

Table 4. The average static contact angle of FOTS and Si oil samples before and after IPA/acetone cleaning.

From these results it can be seen that from all hydrophobic coating types, the static contact angle for PFDTS dropped considerably after the wetting period in water. The static contact angle for FOTS and silicone oil remained the same within the error margin. It is because of this result that the PFDTS was not used as a coating type in our measurements performed in the liquid cell, because a change in the ellipsometry signal could be attributed to the effects related to the observed static contact angle decrease upon extended contact with water. Furthermore, it is observed that FOTS coatings are affected by the IPA/acetone mixture. When taking all these results in consideration, Silicone oil was the most used chemical for hydrophobization, not only due to its resilience to chemical cleaning, as stated by Arayanarakool *et al.* [1], but also due to the relative ease with which it can be made.

3.2 Dynamic scans

During the course of this thesis, several experimental techniques have been tried to test our hypothesis. It was found out eventually that in our case, there are a number of parameters

---

[1] Data of this measurement is not available. The static contact angle of freshly etched silicon oxide samples reach values as low as 5°, while samples that have aged under water for more than 10 hours have a static contact angle of 20-30°. One possible explanation for this increase is due to organic materials being deposited on the surface, another is that dust particles may attach themselves to the surface, increasing roughness, and hence the static contact angle.

that cannot be controlled fully, such as air diffusing in our water-filled liquid cell, or the oxygen (or other gases) concentration at the start of the measurement. Therefore, any other parameters were controlled as much as possible, as explained in section 2.4.3 and 2.4.4 of the Methodology. The dynamic scans were done on both hydrophilic uncoated and silicone oil coated samples in water ambients that differed in their initial compositions of gas. This set of experiments is listed in Table 5.

Sample type	Initial composition of ambient
Uncoated silicon oxide (hydrophilic)	Degassed water
	N_2 saturated water
	He saturated water
Silicone oil coated silicon oxide (hydrophobic)	Degassed water
	N_2 saturated water
	He saturated water

Table 5. The measurement setup used for the dynamic scans.

After each dynamic scan, the ellipsometry data is fitted with the models using the WVASE software. The fitting parameter was the SiO_2 thickness, which as described before is a parameter used to describe change at the solid/water interface. Each dynamic scan is comprised out of a multitude of spectroscopic scans that take 25 minutes. The very first spectroscopic scan is set as the baseline measurement, with a certain fitted SiO_2 thickness. The spectroscopic scans that follow it are analyzed, and the fitted SiO_2 thicknesses are subtracted from the SiO_2 thickness of the initial scan. The result is a normalized fitted SiO_2 thickness curve plotted against the time. The results of the dynamic scans done in the order laid out in the previous table can be seen in Figure 12.

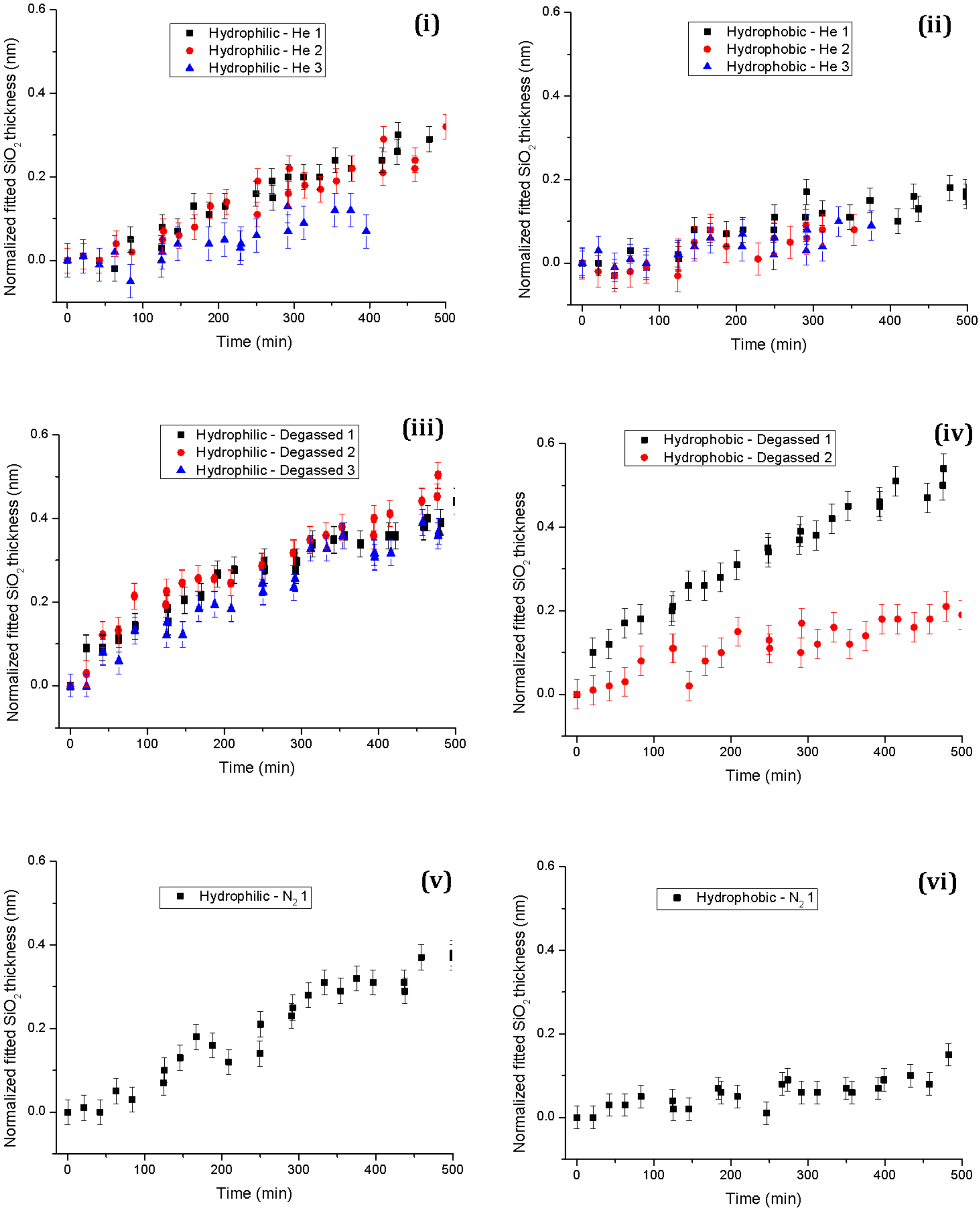

Figure 12. The analyzed measurements from the dynamic scans where data is plotted as the normalized fitted SiO$_2$ thickness (nm) against the time (min). The graphs in (i), (iii), and (v), show the curves for the hydrophilic samples, situated in a He-saturated, degassed, and N$_2$-saturated ambient, respectively. The graphs in (ii), (iv), and (vi), show the curves for the hydrophobic samples, situated in a He-saturated, degassed, and N$_2$-saturated ambient, respectively.

It should be noted that not all the scans have been done three times due to the time limitations. Nonetheless it is possible to discuss the current results. The following section will discuss the graphs depicted in Figure 12.

1) Growth curves for the degassed water ambient tend to increase at a fast rate at the start of the measurement, and slow down until a saturation point is reached, typically after more than 3000 minutes of measurement. See also Figure 13.

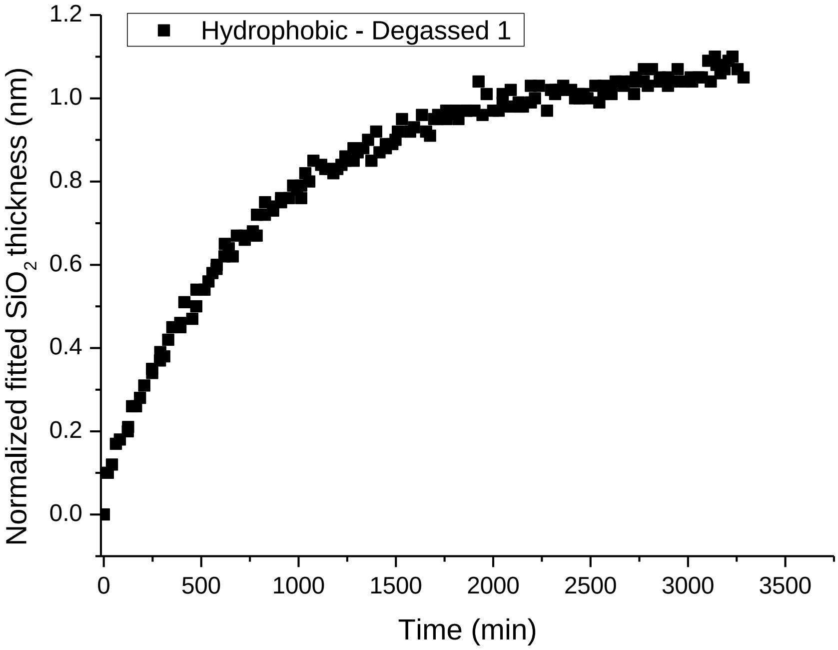

Figure 13. The normalized fitted SiO_2 thickness curve for a long (>3000 minutes) dynamic scan. The measurement was in this case the 1st Hydrophobic – Degassed scan.

2) In the He-saturated water ambient, the growth curve at the start is different: there is an initial time period where there is no growth, or a reduction in fitted SiO_2 thickness (indicated in the dashed red line). This period usually takes 100-150 minutes, after which the growth pattern similar to the degassed water ambient is observed, albeit at a slower pace. See also Figure 14.

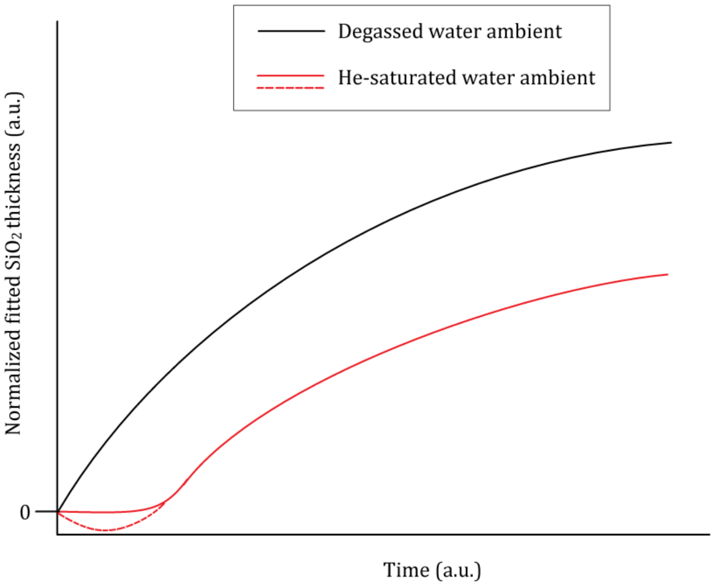

Figure 14. General shape of the growth curves for both hydrophilic and hydrophobic samples in degassed water ambients and He-saturated water ambients.

3) There is a large spread in the growth curves of the hydrophobic samples in the initial degassed water ambient compared to the water exchanged measurements. One explanation is the fact that the measurements done in the degassed water ambient had an initial concentration of oxygen (and therefore, air) that we could not control. The initial value of oxygen typically varied from 20% to 40%. The exchange process controls this to a certain extent, the oxygen saturation at the start was typically held between 6% and 9%. One way to overcome this problem is to exchange the water in the liquid cell, after it is freshly degassed, with degassed water. Due to time restrictions, we could not apply these adjustments.
4) All the curves show a growth in the normalized fitted SiO_2 thickness. The possible reasons for this will be summed up and assessed in section 3.2.2.
5) For the N_2-saturated ambients, there also seems to be an initial time period where there is limited growth of the fitted SiO_2 thickness. For now there is too little data to adequately compare to the He-saturated water ambients.
6) There is a difference in fit data between the hydrophilic and hydrophobic cases. One might expect gas saturation to occur more readily on hydrophobic surfaces than on hydrophilic surfaces due to a depletion layer of water in the hydrophobic case. The growth of fitted SiO_2 thickness for the hydrophilic samples also seems to be larger than for hydrophobic ones. Perhaps this is due to the tendency of hydrophilic surfaces to be contaminated easily. This is also why the contact angle of freshly etched samples change significantly after being wetted with H_2O for several hours.

3.2.1 Delta signal interpretation

To emphasize the effect of He-saturated water on the ellipsometer signal, we can look at the normalized delta plots. The data from the ellipsometer is recorded in two parameters: delta (Δ) and psi (Ψ). When there are changes occurring on the surface (gas layers growing, or contaminations, etc), the delta and psi signals will change over time. Since the delta signal is more sensitive to changes (in our case) compared to the psi, we record the change in delta after each spectroscopic scan, with the first delta signal of the first spectroscopic scan as a reference, see also Figure 15. This is similar to what we did in the normalized fitted SiO_2 curves.

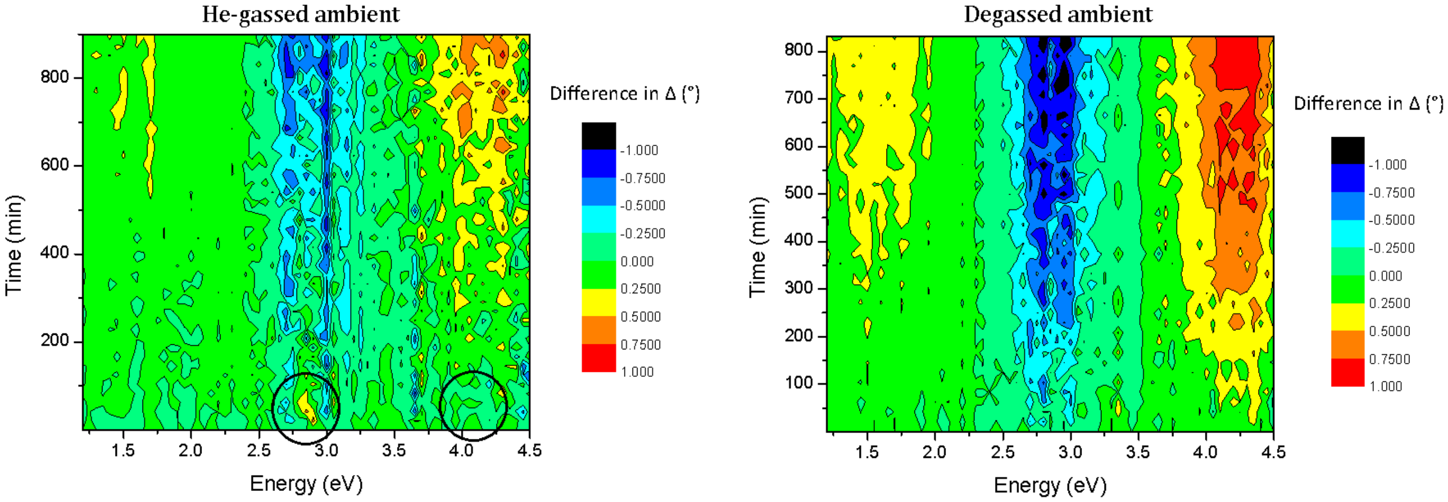

Figure 15. Typical normalized delta plots for measurements (regardless of hydrophobicity) done in He-gassed and degassed water ambients. The black circles indicate the inversion in the shift of delta (i.e. to higher energy).

What is typically seen in the growth curves for measurements in the degassed ambients, is that the normalized delta increases immediately after the start of the measurement, until it equilibrates. The observed change in the normalized delta plot scales linearly with the normalized fitted thickness for very small changes in delta. This is due to the curve of the delta signal, as can be seen in Figure 16.

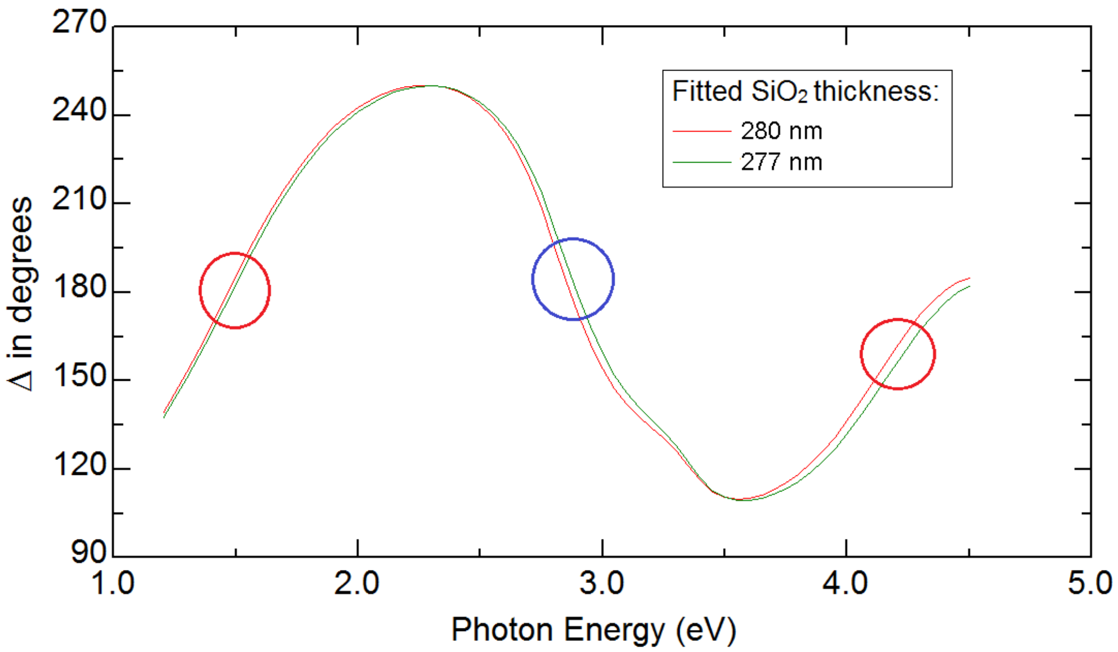

Figure 16. A shift of delta to lower energies implies a positive change (red circle) in the normalized delta at around 1.5 and 4.2 eV, and a negative change (blue circle) at around 2.8 eV. Similarly, a shift of delta to higher energies implies a negative change in the normalized delta at around 1.5 and 4.2 eV, and a positive change at around 2.8 eV.

Any physical change in the top layer will cause the delta signal to shift to higher or lower energies. The delta curve shifts to lower energies mainly depends on whether the modified top layer has a refractive index higher than that of water. If the top layer has a refractive index lower than that of water, the delta curve shifts to higher energies. The effects of these shifts on the normalized delta curve, are shown in Figure 15.

When taking into account the data presented in Figure 14 and Figure 15, it is likely that the inversion in the delta shift in the first 150 minutes, has to do with a modification of the top layer where a layer is added with a refractive index lower than that of water. Again, it is likely that He is enriching the solid/water interface. This also coincides with the normalized fitted SiO_2 thickness curves for the He-saturated measurements, where there is virtually no increase, or even a decrease, in the fitted SiO_2 thickness in the first 150 minutes. Section 5.2 contains more information on the possible causes in the changes found in the fitted SiO_2 thickness.

3.2.2 Reasons for growth in fitted SiO_2 thickness

As can be seen from Figure 12, all the normalized fitted SiO_2 thickness curves are growing eventually over time, there is a limit to this growth, however, as can be seen in Figure 13. The growth of fitted SiO_2 layer can have several reasons.

1) The first reason is that there is enrichment of the solid/water interface with O_2 and N_2 from the air outside the liquid cell. When taking the oximeter data into account, one can notice that the O_2 saturation in water also reaches a maximum eventually, as can be seen in Figure 17.

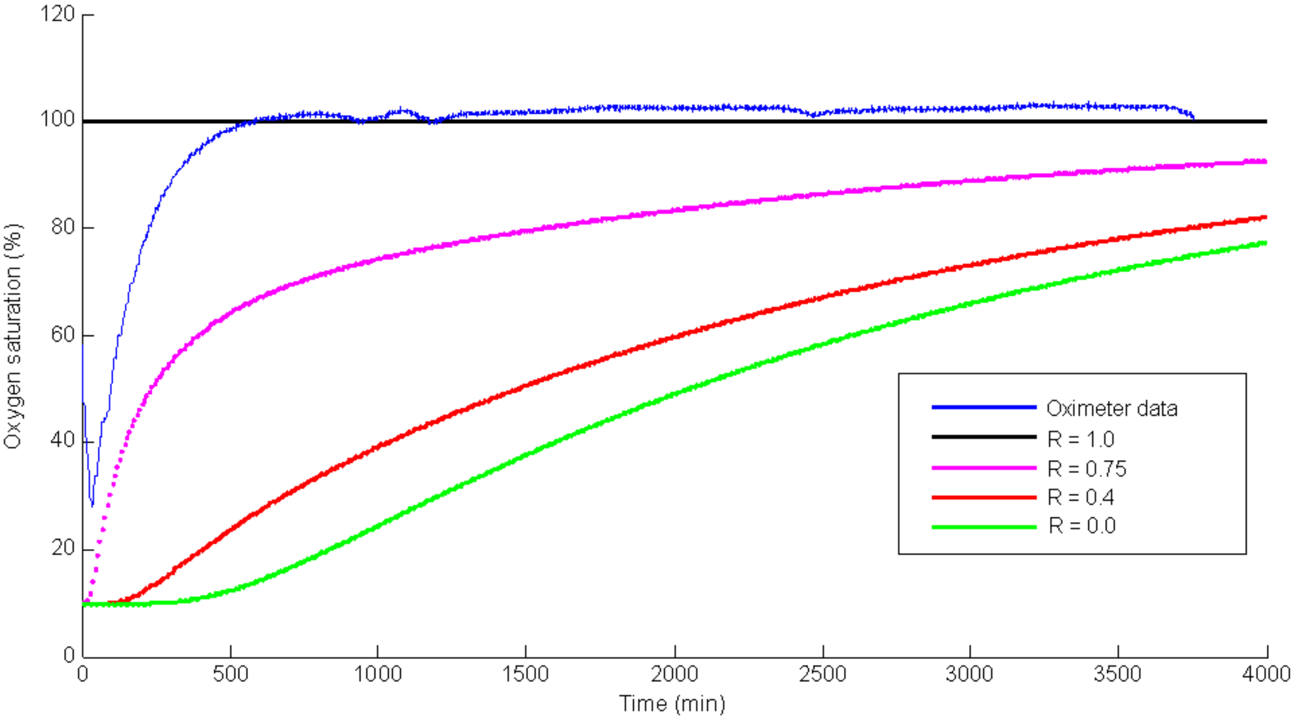

Figure 17. Oxygen saturation profile (%) plotted against measurement time (min). The black, magenta, red, and green curves represent modeling data for different depth ratios, R (see also section 2.5). With the black line representing the oxygen saturation curve at the surface of the water in the liquid cell, and green that of the bottom of the liquid cell. The depth of the measurement spot is represented by the red curve. To compare, the oximeter data at R = 0.4 is plotted and represented by the blue curve.

There is a discrepancy observed between the modeling and the measured data. One possible explanation is that the liquid cell after degassing is carried to be mounted for the measurement. It is during this process that there is shaking involved, increasing the oxygen concentration in the water. Another explanation is due to the temperature differences inside the liquid cell. During degassing, a heater is held beneath the liquid cell, which prevents it from cooling down due to water evaporation. At the bottom, the liquid cell is warmer than at the top. This can cause thermal convection, which also can increase the oxygen concentration. Nevertheless, the oxygen concentration qualitatively resembles the fitted SiO_2 data over time. One way to combine the oximeter and fitted SiO_2 thickness data in an adsorption model, is to use the BET-model, as explained in section 2.6 of Methodology.

The following graph shows the BET-model used for two of our data sets, namely 'Hydrophilic – Degassed 3' and 'Hydrophobic – Degassed 1'. We also fitted these curves with the BET-model and presented them in Figure 18.

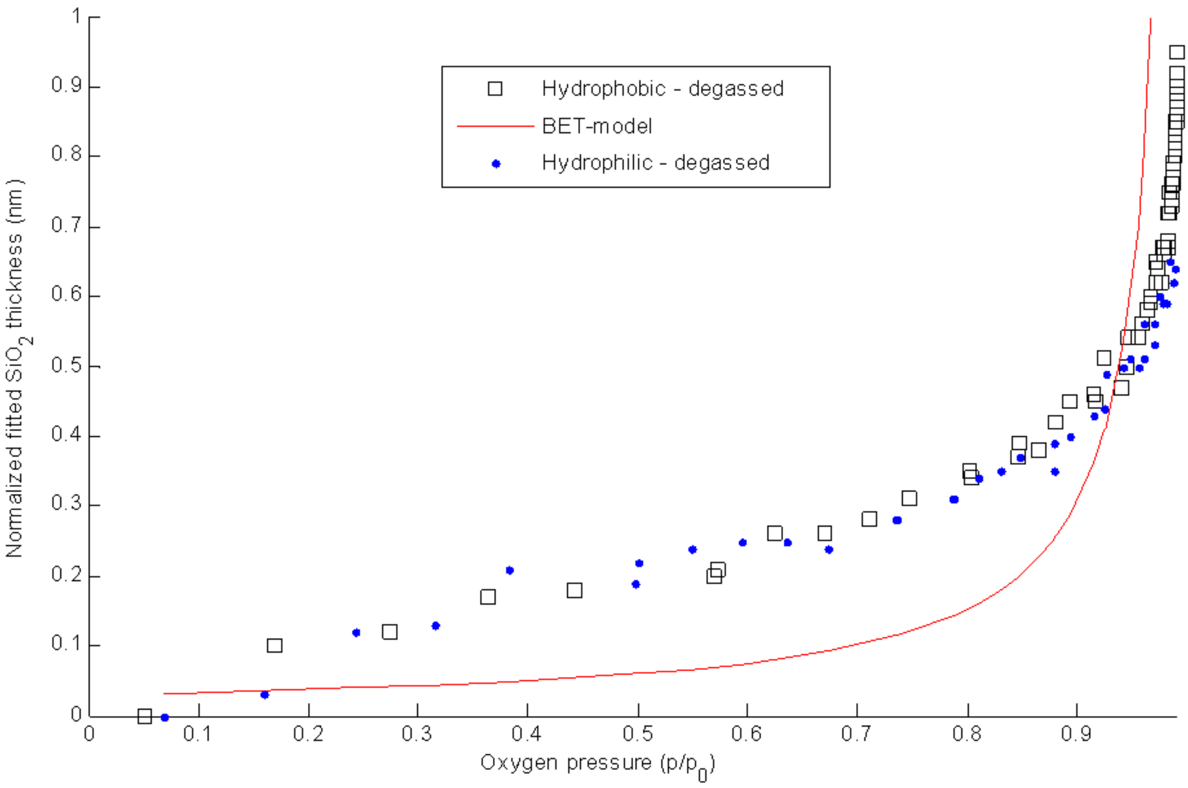

Figure 18. The normalized fitted SiO_2 thickness (nm) data plotted against the oxygen pressure and compared to a BET-model fit.

It should be kept in mind that the BET-model fit in Figure 18 is not necessarily the best fit for these data series. The discrepancies between the plotted data and the model can be explained by the following: to test the BET-model one should keep the p/p_0 constant and let the system equilibrate after which the measurement should be done. In our case, the p/p_0 is constantly changing and there is no equilibrium, except at $p/p_0 = 1$ (when the water in the liquid cell is fully saturated with air after >500 minutes).

2) Another explanation for the long-term increase of the fitted SiO_2 thicknesses as can seen in Figure 12, is due to contaminants adsorbing on the surface. The main reason to consider this explanation is the low refractive index of gases. We have models available for He and N_2 (we will assume N_2 is also a good approximation for O_2, due to the lack of a model available for O_2) gas types. Gaseous He and N_2 in standard atmospheric pressure and room temperature refractive indices of 1 and 1.0003, respectively. According to modeling data in section 5.2 of the Appendix, any added top layer that has a refractive index higher than that of water (refractive index of H_2O lies between 1.3246 (at 1.2 eV) and 1.3659 (at 4.5 eV)), will cause an increase of fitted SiO_2 thickness. For this to occur, the density of N_2 should be higher than approximately 48×10^3 mol/m^3, see also Figure 19. The refractive index of He even at 100×10^3 mol/m^3 is 1.08, so even at extremely high densities, He would still give a lower fitted SiO_2 thickness. To give the reader a comparison, the densities of liquid N_2 and He are 28.8×10^3 and 32.5×10^3 mol/m^3, respectively.

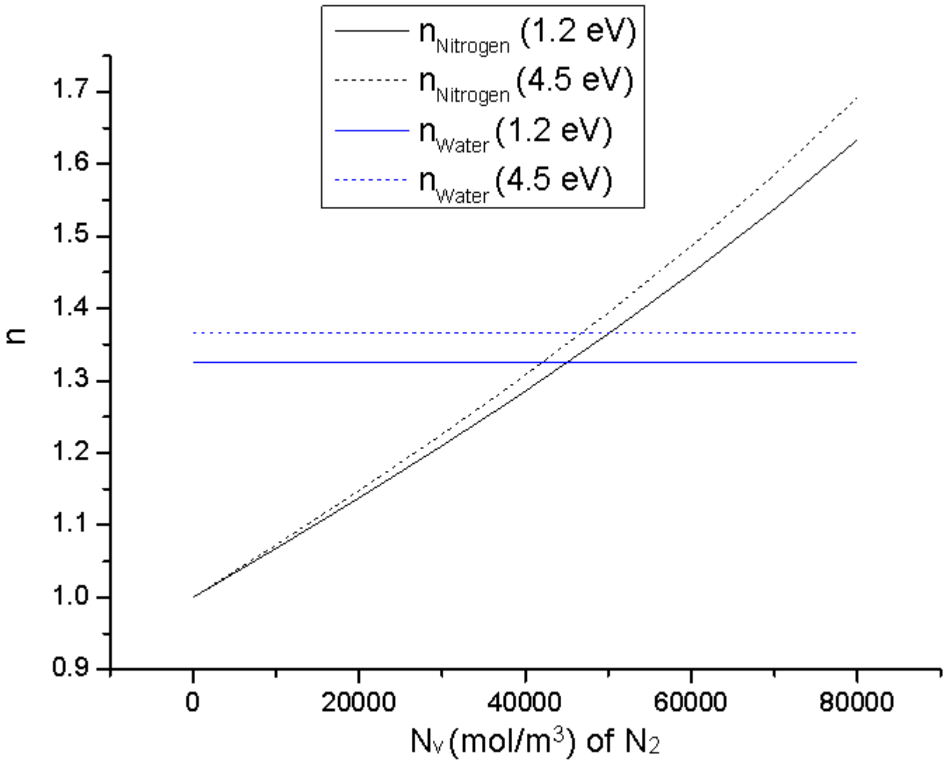

Figure 19. The refractive index of N_2 plotted against its density N_v (mol/m^3). For clarity, a comparison with the refractive index of H_2O is included. The spread in the refractive index due to the energy range used in our measurement data.

Consequently, if air (i.e. N_2 and O_2) diffusing from the water onto the sample surface would be the only factor contributing to the top layer growth, we would have to see a drop in the SiO_2 thickness over time. We do see a stable SiO_2 thickness, or even a drop therein, with He-saturated water. This can be explained with the previous reasoning with the refractive indices.

So what could be causing the increased SiO_2 thickness? One obvious explanation is contaminations from the external environment in the form of organic molecules. Organic substances usually have refractive indices higher than that of water, so adsorbed layers would be interpreted as an increase in SiO_2 thickness. Our system is open for air to diffuse in, but also contaminants that are in the air. Furthermore, the liquid cell and the syringe used for exchanging the water, could potentially be supplying contaminants.

Would this explanation be compatible with the BET-model? The BET-model aims to explain the adsorption of gas molecules on surfaces. This model could also be used to explain organic molecules adsorbing on the surface, however. One point of critique to the contamination hypothesis would be the shape of the curve seen in Figure 13. For contaminations one might expect the layer to be growing continuously over time and without stopping after a certain amount of time has passed.

One other source of change in the fitted SiO_2 thickness could be from CO_2 diffusing in the water. Through chemical reactions, CO_2 could in turn form formic acid (HCOOH) and formaldehyde (CH_2O), which can chemisorb on the silicon oxide surface [3].

3.3 Other sets of data

Other experiments have been made prior to the last series of dynamic scans which have been discussed in section 3.2 of this chapter. These experiments are static scans, and initial dynamic scans done on native oxide. The dynamic scans on native oxide were performed before the process was done consistently as described in section 2.4.3 and 2.4.4 of Methodology. These results will be discussed in section 5.3 and 5.4 of the Appendix.

3.4 Recommendations

To gain a more thorough understanding on the topic of gas-enrichment at the solid/water interface, there are several things one might want to take into consideration for future experiments.

Native oxide samples have not gone through a thorough experimental procedure as the thermal oxide samples. It is worth doing a full investigation on native oxide samples as well. Furthermore, the effect of a substrate different to that of silicon oxide can also be used for investigation. One convenient substrate is HOPG: cleaning is just a matter of cleaving the surface, so chemicals do not have to be used. Furthermore, gaseous domains, such as nanobubbles, have already been found on the HOPG surface when submersed in water. To have a better understanding of the effects of contact angle on the formation, substrates with a wide variety of contact angles can be used in the experimental methods laid out in this thesis.

One uncontrolled parameter was the inevitable diffusion of air (and contaminants) in our system, which can change our ellipsometer signal by enriching the surface. One way to control this parameter by for example using a closed system, or a liquid cell exposed to an atmosphere of only one gas type. This would lead to a higher degree of control and consistency.

One limiting factor related to the ellipsometer used in this thesis, is the time resolution. In the experiments done with the He-saturated water, the effect of He on the ellipsometer signal is noticeable in the first 150 minutes. To have a more detailed information in this time region, it is important to have a higher time resolution than 25 minutes, without compromising the energy resolution.

To investigate the effects of diffusion of gas into our system, we firstly tried stirring our system manually with a metal spoon. Of course, the stirring should be automatized and done consistently. This way, data from the stirring experiments can be taken for a much longer period so that it can be adequately compared to the non-stirring experiments.

Bibliography of Results and discussion

1. *A new method of UV-patternable hydrophobization of micro- and nanofluidic networks.* **R. Arayanarakool, L. Shui, A. van den Berg, J.C.T. Eijkel.** 2011.

2. *Nanobubbles and micropancakes: Gaseous domains on immersed substrates.* **J.R.T. Seddon, D. Lohse.** 133001, s.l. : Journal of Physics: Condensed Matter, 2011, Vol. 23.

3. *Adsorption of methanol, formaldehyde and formic acid on the Si(100)-2x1 surface : A computational study.* **X. Lu, Q. Zhang, M.C. Lin.** 2156-2161, s.l. : Physical Chemistry Chemical Physics, 2001, Vol. 3.

4. Conclusions

In this thesis we have tried to answer the following research questions:

3) *Does gas enrich the solid/water interface?*
4) *Is there a difference in enrichment between hydrophobic and hydrophilic surfaces?*

The following points sum up our most important conclusions based on our research.

- Widely used PFDTS-coated substrates were found unreliable in our experiments due to the changes found in the static contact angle prior and after wetting with water. Si oil coatings were eventually used to hydrophobize the silicon oxide samples.

- Dynamic scans with the ellipsometer were performed on hydrophobic and hydrophilic (thermal) silicon oxide samples in a liquid water ambient, which could be degassed, or gas-saturated with He and N_2. The main proof that gas-enrichment on the solid/water interface is provided by the differences between the fitted SiO_2 growth curves for the He-saturated water ambient and degassed water ambient. In the He-saturated water ambient, there is almost no growth or even a reduction in fitted SiO_2 for the first 150 minutes.

- In the dynamic scans, it was found that for every measurement, there is a long term growth curves for the fitted SiO_2 thickness. The He-saturated water ambient is different in that there is an initial period in which there is no change in the fitted SiO_2 thickness.

- The long-term increase in fitted SiO_2 thickness is likely due to contaminants diffusing from the external environment and adsorbing on the surface.

- There is a difference in the fitted SiO_2 thickness between hydrophilic and hydrophobic surfaces. Hydrophilic surfaces seem to exhibit a larger change in the fitted SiO_2 thickness than the hydrophobic cases. This may be caused by the relatively large tendency of hydrophilic samples to be contaminated, leading to a change in static contact angle.

- When plotting the fitted SiO_2 growth curves against the oxygen partial pressure, a curve very similar to that of a BET-isotherm is found. The BET-isotherms predict multiple gaseous layers adsorbing on the solid surface. This model does not, however, exclude anything else adsorbing on the surface, such as contaminants.

Acknowledgements

I would like to thank all members from the PIN group for their support in the completion of this thesis. In particular, I am grateful for the help and scientific insight of my supervisors Herbert Wormeester and James Seddon, and the leader of the group Harold Zandvliet for his kindness.

From the technicians of PIN I would like Hans and Herman for their kindness and support when I had problems.

I would also like to thank Robin Berkelaar for helping me in the laboratory and for the nice discussions we had.

Lastly, I am very grateful to Dhirendra Tiwari for making time in his busy schedule to teach me how to coat my samples.

5. Appendix

5.1 Hydrophobic coatings

This section will discuss the three mainly used hydrophobic coatings on the investigated silicon sample.

5.1.1 PFDTS

1H,1H,2H,2H-perfluorodecyltrichlorosilane, also known as PFDTS, is a colorless liquid at room temperature, just as the other two chemicals used for hydrophobization in this thesis. In Figure 20, the chemical structure of PFDTS is displayed.

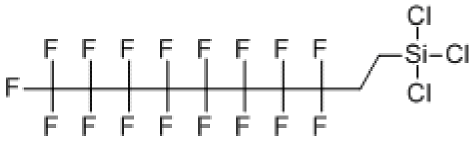

Figure 20. Structural formula of PFDTS [1].

PFDTS is used to form self-assembled monolayers on surfaces with terminated –OH groups, such as silicon oxide. It has been suggested that the formation of PFDTS films on a silicon substrate is due to a combination of both hydrolysis and condensation reactions [2]. The hydrolysis reaction proceeds as follows:

$$R_f - SiCl_3 + H_2O \rightarrow R_f - Si(OH)_3 + 3HCl$$

Which is followed by the condensation reaction:

$$2[R_f - Si(OH)_3] \rightarrow [R_f - Si(OH)_2 - O - Si(OH)_2 - R_f] + H_2O$$

R_f is represented by the rest group of the PFDTS molecule, which is $CF_3(CF_2)_7(CH_2)_2$. The refractive index of PFDTS is 1.349 [3].

5.1.2 FOTS

Trichloro(1H,1H,2H,2H-perfluorooctyl)silane, also known as FOTS, is chemically very similar to PFDTS. In FOTS, there are 6 carbon atoms that have been fluorinated, instead of 8 in PFDTS. It has a refractive index of 1.352 [4]. The chemical structure is shown in Figure 21.

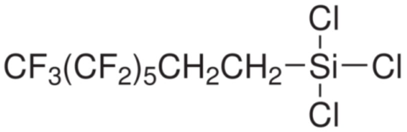

$$CF_3(CF_2)_5CH_2CH_2-SiCl_3$$

Figure 21. Structural formula of FOTS [4].

Like PFDTS, FOTS reacts with the silicone oxide substrate in the same way and methods of producing FOTS and PFDTS coatings proceed similarly.

5.1.3 Silicone oil

Silicone oil is different from the previous chemicals in that it is a polymerized siloxane with organic side groups. An example of the chemical structure of silicone oil is given in Figure 22.

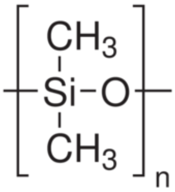

Figure 22. Structural formula of silicone oil [5].

Silicone oil with the structural formula as depicted in Figure 22, has a refractive index is 1.403 [5]. It is not known whether the silicone oil in used in this thesis has the methyl side groups as depicted in Figure 22, thus the refractive index can vary around the given number of 1.403.

While the previous two chemicals are quite reactive to water and require skillful handling in order to conserve it, silicone oil on the other hand is unaffected when exposed to water or oxygen [6]. After plasma cleaning of a silicone sample, there will be Si-O and Si-OH groups available on the surface [7]. When applying silicone oil on top of this layer and after which irradiating it with UV light, the silicone oil molecules can break down. The fragments can react with the Si-OH groups on the silicone oxide surface, resulting in the hydrophobization of the surface [8], due to the apolar nature of the side groups.

5.2 Modeling with WVASE software prior to measurement

The following part in the appendix is mainly about predicting the change in ellipsometric signals when individually adjusting the values of several relevant parameters and variables, such as SiO_2 *thickness, temperature, voids, (nitrogen or helium) gas layers, refractive indices of top layers. The predictive models were made for silicon with a thermal oxide layer. Each time, one parameter is changed marginally, while the other parameters stay constant. The difference in signal is then plotted in the WVASE program.*

The modeling procedures are displayed schematically in Figure 23, 24, and 25. On the left sides of the figures, the model overview is given. The red circles indicate where the changes were made in the model parameters. These individual changes induce a change in the signal of delta, the plots of which are displayed on the right side of the figures. The individual effects of adding a layer of N_2 and He gas (with different densities N_v (mol/m^3)) on top of the SiO_2 substrate will be shown in Figure 23.

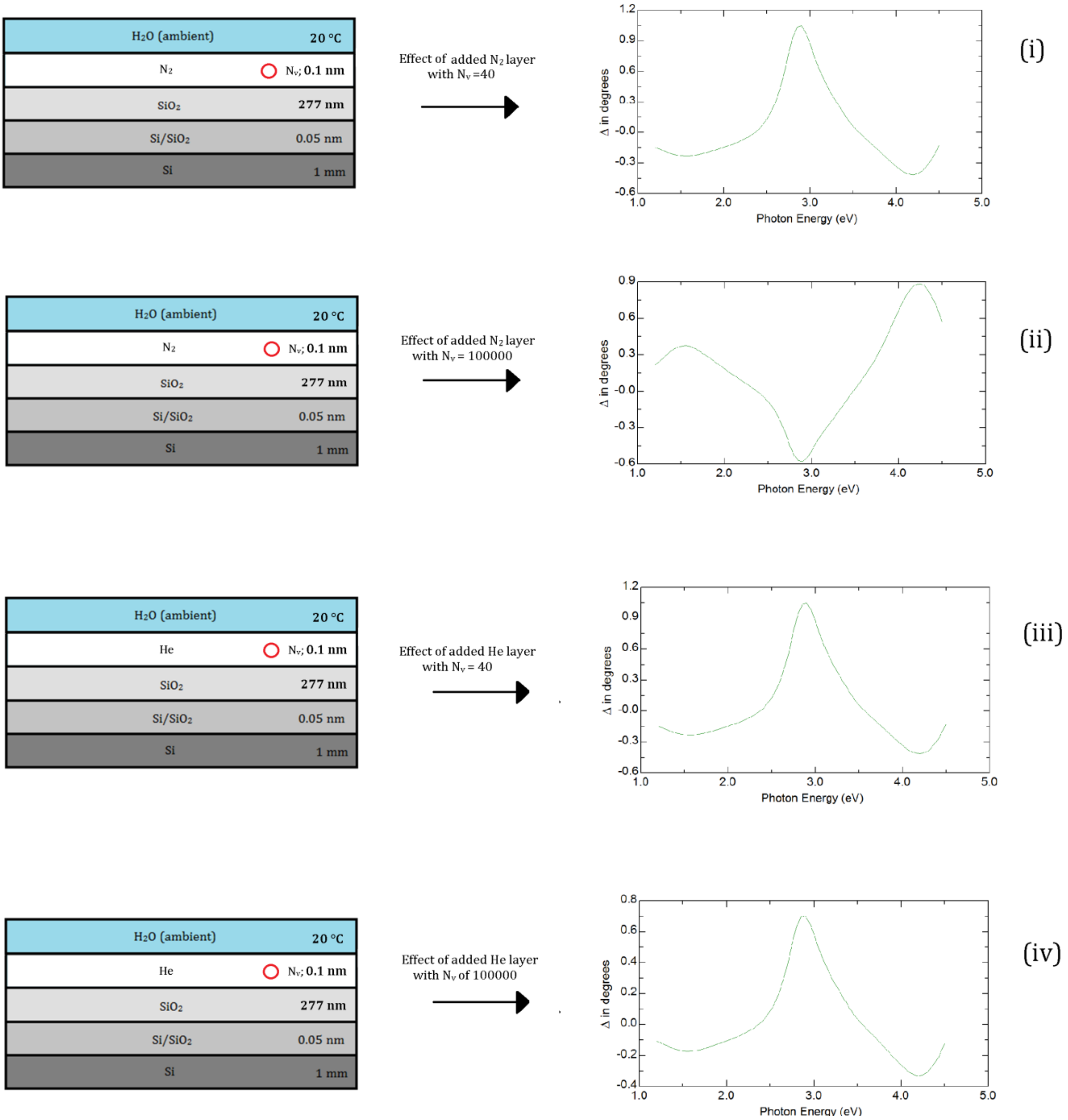

Figure 23. The modeled changes in the delta signal induced by (i), an added N_2 layer with $N_v = 40$ (i.e. gas at atmospheric pressure and 25 °C), (ii), an added N_2 layer with $N_v = 100000$ (higher density than liquid N_2, as a comparison, liquid H_2O has N_v of approximately 55000), (iii), an added He layer with $N_v = 40$, and (iv), an added He layer with $N_v = 100000$ (i.e. more dense than liquid He).

The effects of temperature change, SiO_2 thickness growth, and an added void layer, is represented in Figure 24.

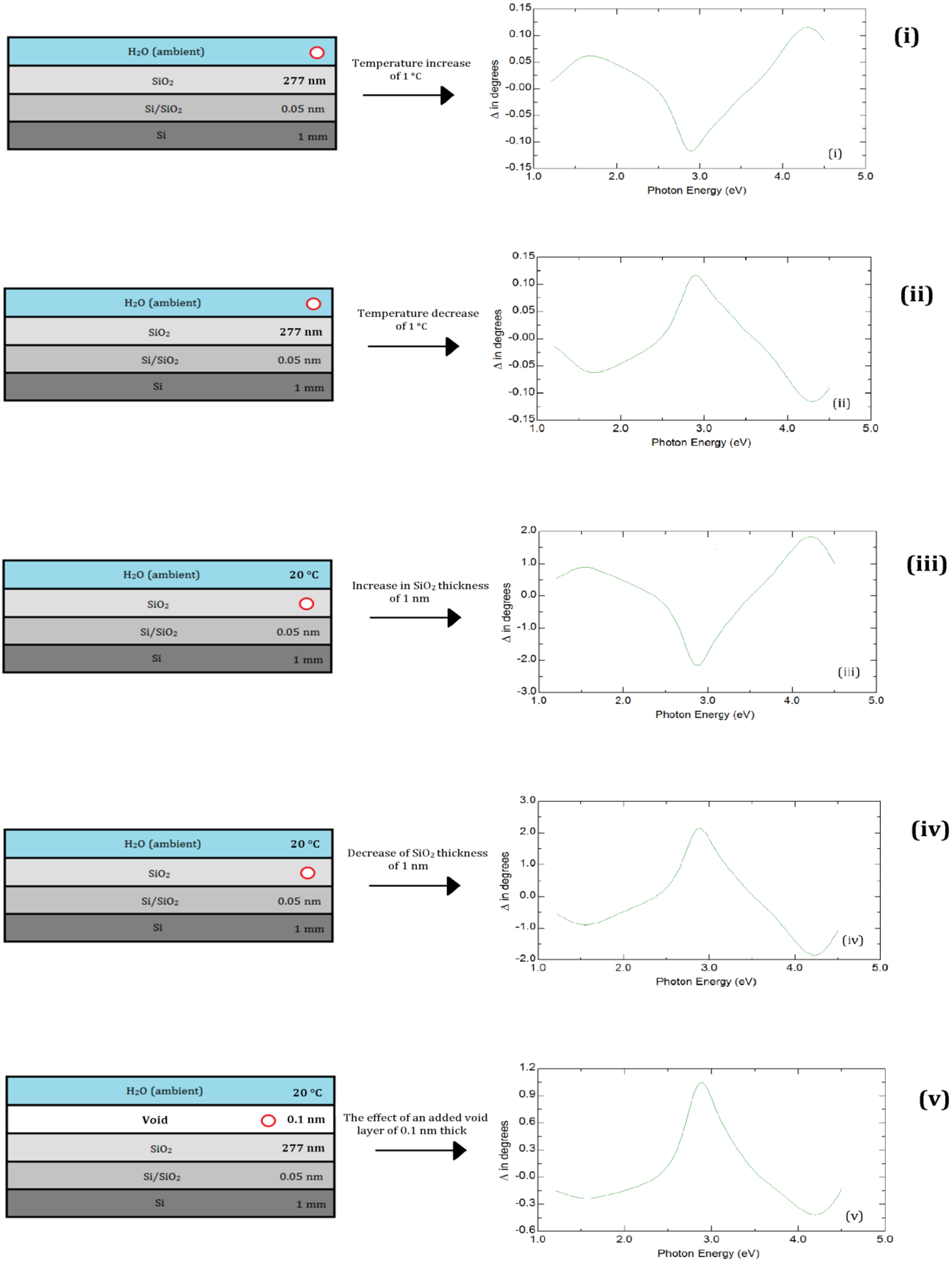

Figure 24. The modeled changes in the delta signal induced by (i), a temperature increase of 1 °C, (ii), a temperature decrease of 1 °C, (iii), an increase of SiO_2 thickness of 1 nm, (iv), a decrease in SiO_2 thickness of 1 nm, and (v), an added void layer of 0.1 nm thick.

Finally, a custom Cauchy layer that resembles water in optical properties is added on top of SiO_2. The refractive index of a Cauchy layer is given by the following formula:

$$n(\lambda) = A_n + \frac{B_n}{\lambda^2} + \frac{C_n}{\lambda^4}$$

The coefficients for a Cauchy layer resembling water is as follows: A_n = 1.3236, B_n = 0.0307, C_n = 9.3×10^{-6}. We then look at the effect of changing the coefficient A_n by +0.1 and by -0.1 (i.e. giving the Cauchy layer higher and lower refractive indices, respectively). These individual effects can be seen in Figure 25.

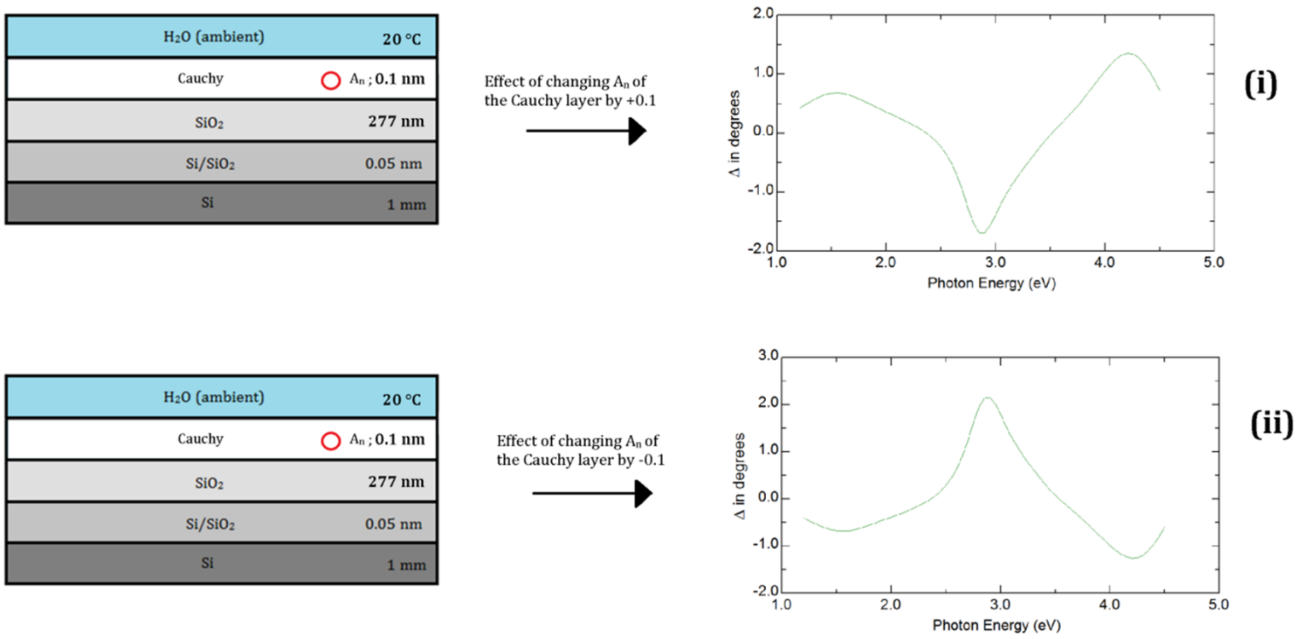

Figure 25. The modeled changes in the delta signal induced by (i), a change in coefficient A_n by +0.1 (i.e. giving the layer a higher refractive index than H_2O), and (ii), a change in coefficient A_n by -0.1 (i.e. giving the layer a lower refractive index than H_2O).

The changes in the delta signal in our case are interpreted as changes in the fit of the SiO_2 thickness as explained previously in section 3.2.1 of the Results and discussion. We will summarize the results of the modeling data in Table 6.

Change in parameter	**Effect in terms of fitted SiO_2 thickness**
Added N_2 with $N_v = 40$ mol/m^3	Decrease
Added N_2 with $N_v = 100000$ mol/m^3	Increase
Added He with $N_v = 40$ mol/m^3	Decrease
Added He with $N_v = 100000$ mol/m^3	Decrease
Temperature increase of 1 °C	Increase
Temperature decrease of 1 °C	Decrease
SiO_2 thickness increase of 1 nm	Increase
SiO_2 thickness decrease of 1 nm	Decrease
Added void layer of 0.1 nm	Decrease
Increase in A_n coefficient by 0.1	Increase
Decrease in A_n coefficient by 0.1	Decrease

Table 6. Correlation between changes in certain parameters in the model and its effect in terms of fitted SiO_2 thickness.

5.3 Spectroscopic scans

The results of the spectroscopic scans will be presented and discussed in this section.

The measurement procedure for the spectroscopic scans is as follows: the first spectroscopic scan was done right after the water-filled liquid cell with sample was degassed. After this measurement, labeled as ‘D (as in degassed)’, the water was replaced with N_2-saturated water and labeled as ‘G (as in gas-saturated)’, and then followed up by a replacement with degassed water labeled as ‘D’, etc. This is the measurement cycle done for all scans. Extra details on how the spectroscopic scans were made, are shown in section 2.4.2 of Methodology.

The spectroscopic scans were performed firstly with the pouring method. Three different samples were used. The uncoated thick oxide sample was hydrophilic, while the FOTS and Si oil coated samples were hydrophobic. These results can be seen in Figure 26. Note that for clarity, the vertical axis of the graphs can be in terms of the absolute fitted SiO_2 thickness, instead of the normalized fitted SiO_2 thickness.

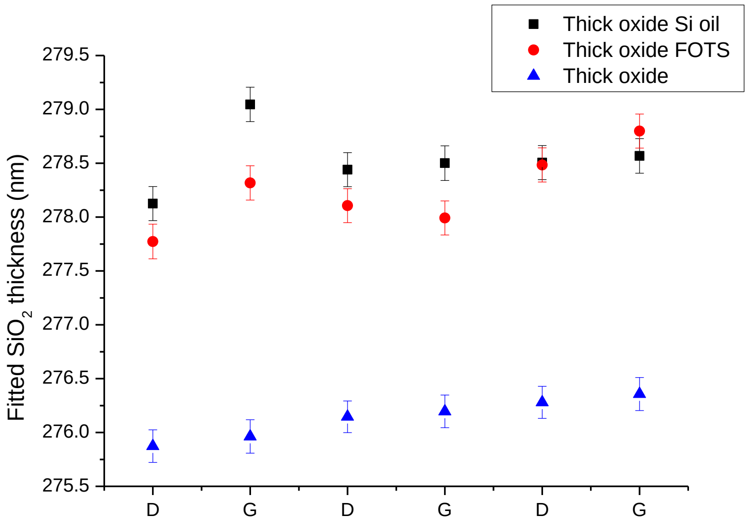

Figure 26. Fitted SiO_2 thickness (nm) plotted against the different water ambients used with the pouring method.

The results using the water-exchange method are shown in Figure 27.

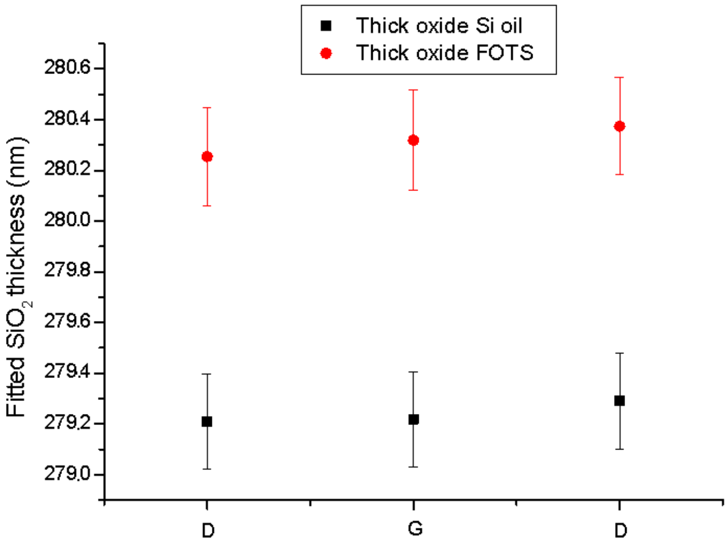

Figure 27. Fitted SiO_2 thickness for the different ambients used with the water-exchange method.

The results using the injection method are shown in Figure 28.

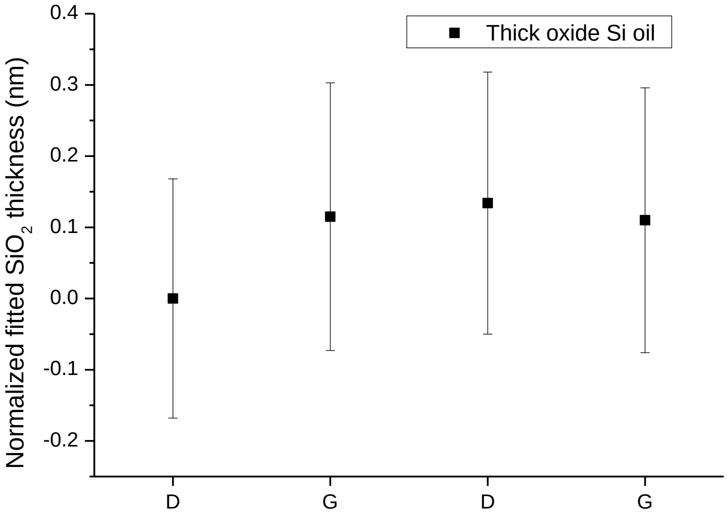

Figure 28. Normalized fitted SiO_2 thickness for the different ambients used with the injection method.

It can be noticed that there are large variations in fitted SiO_2 thickness for the pouring method. This is perhaps due to contaminations that are being introduced on the surface during the pouring. The water-exchange and the injection methods keep the sample wettied, and large variations in thickness as in the pouring method were not observed. We would expect in the ideal case to be a clear, consistent difference in fitted SiO_2 thickness when comparing N_2-gassed ambients and degassed ambients. The exact reason why it does not occur is not clear.

5.4 Preliminary results on native oxide

Dynamic scans were made on native oxide substrates just as the thick oxide substrates. There are differences in the normalized delta plots when the fitted SiO_2 thickness varies for native oxide. There is much larger varation in delta in the region between 1.2 and 1.5 eV, but the error margins in this region are also larger than for the thick oxide measurements. The reason why we did not expand upon native oxide as much as thick oxide, is due to the limited time frame of this thesis. The dynamic scans done on hydrophilic and hydrophobic native oxide samples with the normalized fitted SiO_2 thickness plot is shown in Figure 29.

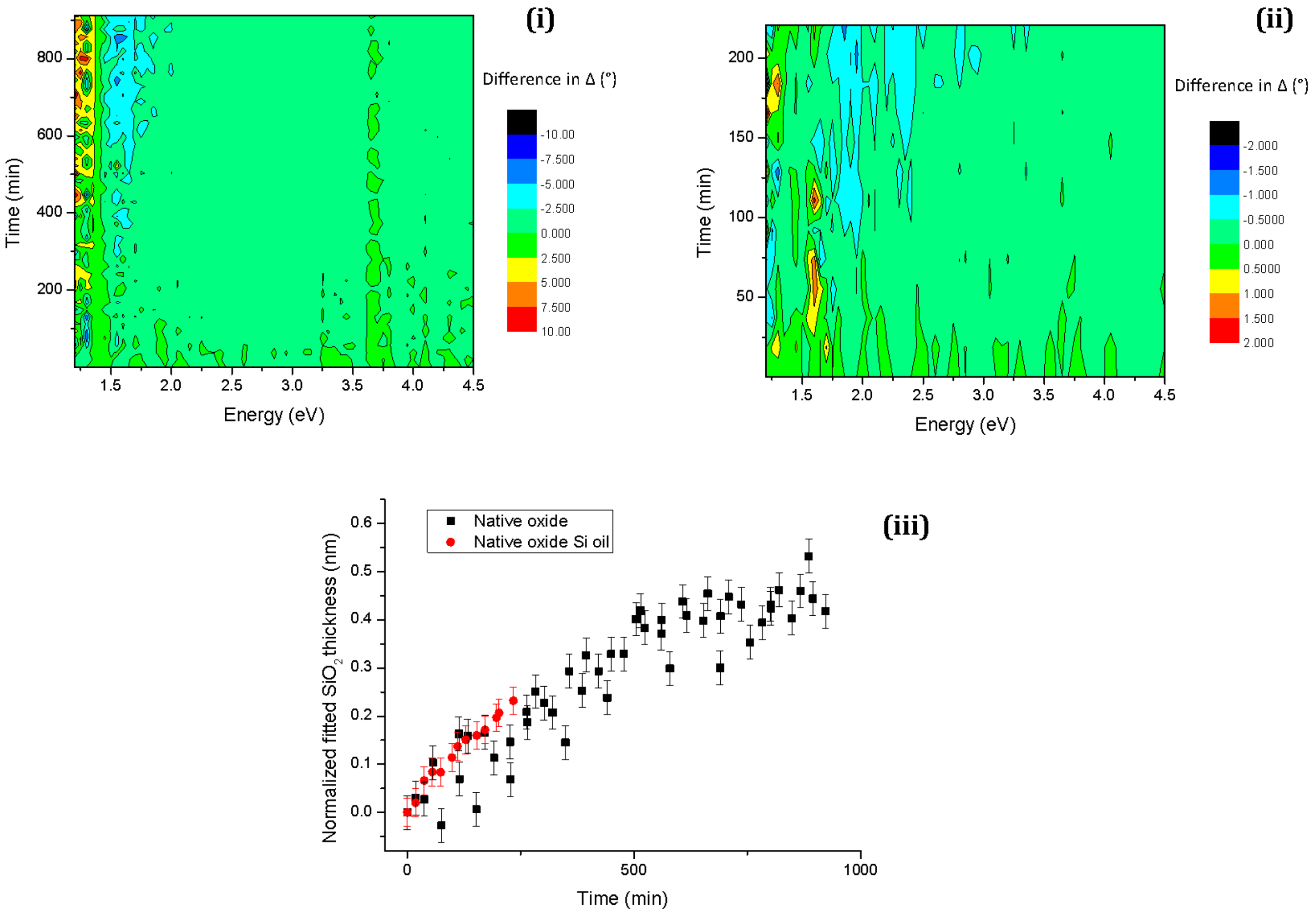

Figure 29. Normalized delta plots for (i) uncoated hydrophilic native oxide and (ii) native oxide coated with Si oil. The normalized fitted SiO_2 thickness plot is shown in (iii).

According to preliminary data shown in Figure 29, the hydrophobic sample shows a slightly larger change in SiO_2 thickness fit than the hydrophilic sample in a degassed ambient. For a good comparison with the thick oxide measurements, a variety in gas-saturated ambients should be used to see if there is also an indication of gas-saturation at the solid/water interface.

Bibliography of Appendix

1. *Chemical Book.* [Online] Fuxin Hengtong Fluorine Chemicals Co., Ltd. http://www.chemicalbook.com/ProductChemicalPropertiesCB2296117_EN.htm.

2. *Superhydrophobicity of Self-Assembled PFDTS Nanostructures.* **M.A. Raza, E.S. Kooij, A. Silfhout, B. Poelsema.** 81-84, s.l. : Progress in Colloid and Polymer Science, 2011, Vol. 138.

3. *Chemical Book.* [Online] Fuxin Hengtong Fluorine Chemicals Co., Ltd. http://www.chemicalbook.com/ChemicalProductProperty_EN_CB2296117.htm.

4. *Sigma-Aldrich.* [Online] http://www.sigmaaldrich.com/catalog/product/aldrich/448931?lang=en&region=NL.

5. *Sigma-Aldrich.* [Online] http://www.sigmaaldrich.com/catalog/product/aldrich/317667?lang=en&region=NL.

6. *A new method of UV-patternable hydrophobization of micro- and nanofluidic networks.* **R. Arayanarakool, L. Shui, A. van den Berg, J.C.T. Eijkel.** 2011.

7. *Improvement on hydrophilic and hydrophobic properties of glass surface treated by nonthermal plasma induced by silent corona discharge.* **T. Yamamoto, M. Okubo, N. Imai, Y. Mori.** s.l. : Plasma Chemistry and Plasma Processing, 2004, Vol. 24.

8. *Preparation of hydrophobic coating on glass surface by dielectric barrier discharge using a 16 kHz power supply.* **C. Want, X. He.** 8348-8351, s.l. : Applied Surface Science, 2006, Vol. 252.